PHYSICAL REVIEW A **109**, 043104 (2024)

Circularly polarized RABBITT applied to a Rabi-cycling atom

Yijie Liao,[1] Edvin Olofsson,[2] Jan Marcus Dahlström,[2,*] Liang-Wen Pi,[3] Yueming Zhou,[1,†] and Peixiang Lu[1,4]
[1]*School of Physics and Wuhan National Laboratory for Optoelectronics, Huazhong University of Science and Technology, Wuhan, 430074, China*
[2]*Department of Physics, Lund University, Box 118, SE-221 00 Lund, Sweden*
[3]*Center for Attosecond Science and Technology, Xi'an Institute of Optics and Precision Mechanics of the Chinese Academy of Sciences, Xi'an 710119, China*
[4]*Optics Valley Laboratory, Hubei 430074, China*

(Received 18 December 2023; accepted 16 February 2024; published 3 April 2024)

We utilize the reconstruction of attosecond beating by interference of two-photon transitions (RABBITT) technique to study the phase of a Rabi-cycling atom using circularly polarized extreme ultraviolet and infrared fields, where the infrared field induces Rabi oscillations between the $2s$ and $2p$ states of lithium. Autler-Townes splittings are observed in sidebands of the photoelectron spectra and the relative phases of outgoing electron wave packets are retrieved from the azimuthal angle. In this RABBITT scheme, more ionization pathways beyond the usual two-photon pathways are required. Our results show that the polar-angle-integrated and polar-angle-resolved RABBITT phases have different behaviors when the extreme ultraviolet and infrared fields have co- and counter-rotating circular polarizations, which are traced back to the different ionization channels according to the selection rules in these two cases and their competition relying on the propensity rule in laser-assisted photoionization.

DOI: 10.1103/PhysRevA.109.043104

I. INTRODUCTION

Rabi oscillations [1] are ubiquitous in nuclear physics [2], atomic physics [3–5], condensed-matter physics [6], and quantum information science [7]. In the semiclassical interpretation, when a single atom is radiated by a laser field that is nearly resonant with the transition from the ground state to an excited bound state [8], the population is periodically transferred via absorption and stimulated emission of a photon [9]. Furthermore, when Rabi oscillations are measured by light-induced perturbative or nonperturbative transitions to *another* bound or continuum state, Autler-Townes (AT) splittings [10] are manifested in the energy domain [11–19], in analogy with Ramsey interference [20,21] from the energy domain to the time domain. The formation of the AT splitting separated by the Rabi frequency Ω_R can be understood by the quasi-eigenenergies in Floquet theory [22,23]. In the Jaynes-Cummings model, the spectral AT doublet is observed when the atom-field interaction splits a pair of near-degenerated "unperturbed" states [24,25].

With the advent of attosecond extreme ultraviolet (XUV) pulses [26,27], attosecond pump-probe spectroscopy enables monitoring and controlling the electronic motion on its natural timescale [28]. For instance, the RABBITT technique is widely employed to investigate the electronic dynamics in laser-assisted photoionization of atoms [29,30], molecules [31], solids [32], and liquids [33]. In conventional RABBITT measurements, an XUV attosecond pulse train (APT) ionizes a target synchronized with a weak infrared (IR) probe field [34,35]. Owing to the interference between the outgoing electron wave packets, the photoelectron yield of sidebands (SBs) located between the main peaks oscillates with the time delay between the XUV and IR fields [27,36,37]. From the modulations of the SB signals, the relative phase of the ionized electron wave packets can be retrieved, which contains two contributions, the phase of the laser fields [27,38] and the phase related to the electronic dynamics in laser-matter interaction [35,39–42].

In the conventional RABBITT scheme with resonant two-photon ionization of atoms, photoelectrons are ionized from the solely populated ground state and an abrupt phase variation around the resonance is observed in SB modulations [43–45]. Recently, the RABBITT simulations on a lithium atom have revealed AT splittings in the SB signals of the photoelectron spectra when the IR field induces several cycles of Rabi oscillations in the atom [13]. During each Rabi cycle on the femtosecond timescale, electrons are periodically transferred between the ground ($2s$) and excited ($2p$) states of lithium [13]. Meanwhile, a train of attosecond XUV bursts assisted with the IR field samples this Rabi process by simultaneously releasing the electrons from *both* Rabi states every half IR period. Hence, the *out-of-phase* feature of the temporal Rabi flopping is imprinted in the spectral interference pattern of the emitted electron wave packets in this self-referenced interferometry. Most interestingly, it is revealed that this Rabi process leads to a near π phase difference in SB modulations between the AT doublet in both angle-integrated and angle-resolved

---

[*] marcus.dahlstrom@matfys.lth.se
[†] zhouymhust@hust.edu.cn

[46] spectroscopies [13]. This real-time evolution of the structured Rabi wave packets below the ionization threshold is out of reach in the previous pump-probe schemes where only *one* of the two Rabi states is measured [11,16,17]. In addition, the influence of the ongoing Rabi oscillations on the *phase* of the outgoing electron wave packets cannot be uncovered by a one-color scheme where only an asymmetric AT doublet is observed at a resonant laser frequency [12].

During Rabi oscillations, the atom is polarized by the resonant IR field and its dipole moment oscillates at the Rabi frequency Ω_R and beats at the energy spacing of the two Rabi states. In the previous streaking [47–49] and RABBITT measurements [50], it was revealed that a permanent dipole moment of a polar target (either in its initial or ionic states) leads to an additional term in the phase of the outgoing electron wave packet. Meanwhile, the induced dipole moment related to the target's polarizability only distorts the shape of the modulation in the streaking spectrum [47]. However, because there are no conceptual counterparts like permanent dipole moment nor polarizability in the case of Rabi oscillations [51], the influence of the Rabi process on the phase of the ejected electron wave packets is investigated by comparing the two peaks in the AT doublet.

In this work, we revisit the RABBITT process of a Rabi-cycling lithium atom and adopt circularly polarized XUV [52] and IR fields to avoid scanning the time delay between the two laser fields [53–55]. In this single time-delay RABBITT measurement, the relative phases of outgoing electron wave packets are retrieved from the photoemission anisotropy along the azimuthal direction. This relative phase encodes the information about the temporal Rabi dynamics in spite of the contamination related to the bound-free and free-free transitions in RABBITT measurements [35]. In accordance with our previous work [13], a near π phase difference *related to the Rabi dynamics* is observed between each pair of splitting SBs in AT doublets for both polar-angle-integrated and polar-angle-resolved photoelectron spectroscopies. Furthermore, the ionization channels are controlled by using co- or counter-rotating XUV and IR fields according to the dipole selection rules, as an advantage of utilizing circularly polarized fields. Correspondingly, the polar-angle-integrated and polar-angle-resolved RABBITT phases exhibit different behaviors due to different competition among partial waves. To give a quantitative interpretation of this complex RABBITT process, more ionization pathways with important roles are considered in perturbation theory than the previous work [13], which elaborates the modification on the Rabi-related phase by the measurement process.

This paper is structured as follows: In Sec. II, we describe the numerical methods in our calculations, including the atomic parameters (Sec. II A) and the numerical details (Sec. II B). In Sec. III, we introduce the theoretical model, including the perturbative treatment of the ionization amplitudes on the top of the Rabi model (Sec. III A), the description of the ionization pathways (Sec. III B), and the review of the RABBITT scheme using circularly polarized laser fields (Sec. III C). In Sec. IV, we present the numerical results, including the corotating case in Sec. IV A and the counter-rotating case in Sec. IV B. We finish with a summary in Sec. V. The paper is completed by Appendix A, which details the derivation of the wave function for the Rabi process; Appendix B, which gives the derivation of the Dyson series for the RABBITT measurement on the Rabi process; Appendix C, which supplements the formulas of the amplitudes for less contributing ionization pathways; and Appendix D, which selects some numerical results of the dipole transition matrix elements for readers' reference. Atomic units are used throughout this paper unless otherwise stated.

TABLE I. The energies of the $2s$, $2p$, $3s$, and $3d$ states of the lithium atom calculated using the effective potential from Ref. [56].

Bound state	Energy (eV)
$2s$	−5.3821
$2p$	−3.7114
$3s$	−2.1822
$3d$	−1.7960

II. METHODS

A. Atomic parameters

In this work, we consider a lithium atom to study the *Rabi-RABBITT* scheme, where the IR field is resonantly tuned to the transition between the $2s$ $(m=0)$ $(|\psi_{2s}\rangle)$ and $2p$ $(m=1$ or $m=-1)$ $(|\psi_{2p}\rangle)$ states of lithium and thus induces the Rabi oscillations between these two states. The lithium atom has a single electron outside a closed shell and thus the single-active-electron approximation is reasonable for describing the photoionization of the lithium atom. In this study, we adopt the one-electron effective potential of the lithium atom from Ref. [56] for the time-dependent Schrödinger equation (Sec. II B) and for perturbative calculations (Sec. III A). Using this model potential, the calculated energies of the $2s$, $2p$, $3s$, and $3d$ states of the lithium atom are given in Table I. Note that in this model, the energy spacing between the $2s$ and $2p$ levels is 1.6707 eV. It deviates from the experimental value given in NIST by 0.1771 eV [57].

Figure 1 shows the photoionization cross sections as a function of the photoelectron energy for the $2s$ and $2p$ $(m=0)$ states of the lithium atom ionized by a linearly polarized laser field. As shown, the photoionization cross sections both decrease monotonically with the photoelectron energy, but the cross section of the $2p$ state decreases faster than that of the $2s$ state. The photoionization cross section of the $2p$ state is larger (smaller) than that of the $2s$ state below (above) the photoelectron energy of around 4 eV. For the laser parameters in our Rabi-RABBITT scheme, we focus on the SBs of the photoelectron energies ranging from 10 to 30 eV, where single-photon ionization from the $2s$ state dominates over that of the $2p$ state by less than an order of magnitude.

B. Time-dependent Schrödinger equation

To uncover the effects of Rabi oscillations on the phase of the ejected wave packet, we solve the time-dependent Schrödinger equation (TDSE) for the lithium atom. The

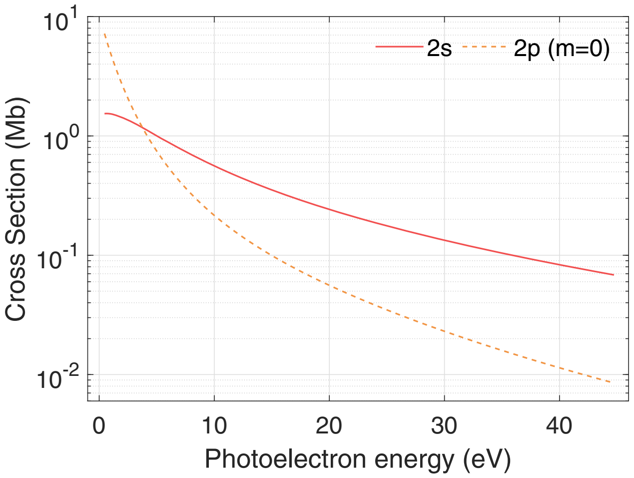

FIG. 1. Photoionization cross sections from the $2s$ and $2p$ ($m = 0$) states of the lithium atom as the functions of the photoelectron energy.

TDSE is written as

$$i\frac{\partial\Psi(\mathbf{r},t)}{\partial t} = \left[H_0 + H_{\text{int}}^{\text{V}}(t)\right]\Psi(\mathbf{r},t), \tag{1}$$

where the atomic Hamiltonian is $H_0 = \mathbf{p}^2/2 + V(\mathbf{r})$. Here the canonical momentum operator of the electron is $\mathbf{p} = -i\nabla$ and $V(\mathbf{r})$ is the effective one-electron potential of the lithium atom [56]. The atom-field interaction term is written in velocity gauge as $H_{\text{int}}^{\text{V}}(t;\tau) = \mathbf{A}(t;\tau)\cdot\mathbf{p}$, where the external laser field is described as

$$\mathbf{A}(t;\tau) = \mathbf{A}_{\text{IR}}(t;\tau) + \mathbf{A}_{\text{XUV}}(t). \tag{2}$$

Here $\mathbf{A}_{\text{IR}}(t;\tau)$ and $\mathbf{A}_{\text{XUV}}(t)$ are the vector potentials of the IR and XUV fields, respectively, and τ is the time delay between the two fields. In our coordinates, the polarizations of both fields are within the zOx plane and they propagate in the y direction. The vector potential of the time-delayed IR field is expressed as

$$\begin{aligned}\mathbf{A}_{\text{IR}}(t;\tau) = {}& \frac{A_\omega \Lambda_{\text{IR}}^{\text{A}}(t;\tau)}{\sqrt{1+\xi^2}}\{\sin[\omega(t-\tau)]\hat{e}_z \\ & - \xi\cos[\omega(t-\tau)]\hat{e}_x\},\end{aligned} \tag{3a}$$

with the envelope function

$$\Lambda_{\text{IR}}^{\text{A}}(t;\tau) = \begin{cases} \frac{1}{2} - \frac{1}{2}\cos\left[\frac{\pi(t-\tau+\tau_{\text{IR}})}{2T}\right], & -\tau_{\text{IR}} < t-\tau < -\tau_{\text{IR}} + 2T \\ 1, & -\tau_{\text{IR}} + 2T \leqslant t-\tau \leqslant \tau_{\text{IR}} - 2T \\ \frac{1}{2} - \frac{1}{2}\cos\left[\frac{\pi(t-\tau-\tau_{\text{IR}})}{2T}\right], & \tau_{\text{IR}} - 2T < t-\tau \leqslant \tau_{\text{IR}} \\ 0, & \text{otherwise.} \end{cases} \tag{3b}$$

Here A_ω is the amplitude of the field, and $\hat{e}_x$ and $\hat{e}_z$ are the unit vectors along the x and z axes, respectively. In our numerical simulations, the central frequency $\omega = 1.6707$ eV is used for the IR field, which corresponds to a period of $T = 2\pi/\omega = 2.4963$ fs. The duration of the IR field is $2\tau_{\text{IR}} = 160T = 399.4080$ fs, corresponding to a spectral width of 0.023 eV. The vector potential of the XUV field is modeled as an APT [44]

$$\begin{aligned}\mathbf{A}_{\text{XUV}}(t) = {}& \sum_{n=-120}^{120} \frac{A_0 \Lambda_{\text{APT}}^{\text{A,(n)}} \Lambda_{\text{XUV}}^{\text{A,(n)}}(t)}{\sqrt{1+\xi^2}} \sin[\omega_{\text{XUV}}(t-nT/2)]\hat{e}_z \\ & - \xi\cos[\omega_{\text{XUV}}(t-nT/2)]\hat{e}_x\},\end{aligned} \tag{4a}$$

where the relative amplitude of the nth XUV pulse in the pulse train is

$$\Lambda_{\text{APT}}^{\text{A,(n)}} = \exp\left[-2\ln 2\frac{(nT/2)^2}{\tau_{\text{APT}}^2}\right], \tag{4b}$$

and the envelope function of the nth XUV pulse is

$$\Lambda_{\text{XUV}}^{\text{A,(n)}}(t) = (-1)^n \exp\left[-2\ln 2\frac{(t-nT/2)^2}{\tau_{\text{XUV}}^2}\right]. \tag{4c}$$

Here A_0 is the amplitude of the field. In our simulations, the central frequency $\omega_{\text{XUV}} = 15\omega$ is used for the XUV field. $\tau_{\text{XUV}} = 0.08T = 0.1997$ fs and $\tau_{\text{APT}} = 50T = 124.8150$ fs are the durations of the XUV attosecond pulses and the APT, respectively. The spectral width of the XUV field is 0.021 eV. In our calculations, both the IR and XUV fields are circularly polarized, with $\xi = -1$ and $\xi = +1$ corresponding to right- and left-hand circularly polarized laser fields, respectively.

The wave function of the TDSE is expanded as a partial wave series

$$\Psi(\mathbf{r},t) = \sum_{l=0}^{l_{\text{max}}} \sum_{m=-m_{\text{max}}}^{m_{\text{max}}} \frac{R_{l,m}(r,t)}{r} Y_{l,m}(\theta,\varphi), \tag{5}$$

where $R_{l,m}(r,t)$ is the radial part of the wave function and $Y_{l,m}(\theta,\varphi)$ are spherical harmonics with polar angle θ and azimuthal angle φ. The angular-momentum quantum number and the magnetic quantum number are denoted as l and m, respectively.

In our calculations, $R_{l,m}(r,t)$ is discretized by the finite-element discrete variable representation method [58], where the box size is $r_{\text{max}} = 400$ a.u.. The numerical convergence is guaranteed with $l_{\text{max}} = 15$ and $m_{\text{max}} = 5$. The initial state of the lithium atom is obtained by imaginary-time propagation. The time propagation of the wave function $\Psi(\mathbf{r},t)$ is implemented by the split-Lanczos method [59,60] with the time step $\Delta t = 0.02$ a.u.. In each propagation step, we apply an absorbing mask function, $F(r) = 1 - 1/[1 + e^{(200.0-r)/2.0}]$, which splits the wave function $\Psi(\mathbf{r},t)$ into the inner part $\Psi_{\text{in}}(\mathbf{r},t) = F(r)\Psi(\mathbf{r},t)$ and the outer part $\Psi_{\text{out}}(\mathbf{r},t) = [1 - F(r)]\Psi(\mathbf{r},t)$. The inner part $\Psi_{\text{in}}(\mathbf{r},t)$ is kept in the propagation governed by the full Hamiltonian $H_0 + H_{\text{int}}^{V}(t)$ and the outer part $\Psi_{\text{out}}(\mathbf{r},t)$ is approximately propagated by Coulomb-Volkov propagator [61]. Specifically, the ionization amplitude of the photoelectrons with the momentum $\mathbf{k}$ at time t_i is obtained by projecting the outer part $\Psi_{\text{out}}(\mathbf{r},t_i)$ on the set of Volkov states as

$$f(\mathbf{k},t_i) = \left\langle \psi_{\mathbf{k}}^{\text{V}}(\mathbf{r},t_i) \middle| \Psi_{\text{out}}(\mathbf{r},t_i) \right\rangle. \tag{6a}$$

Then the total ionization amplitude at the final time t_f is expressed as

$$f(\mathbf{k}) = \sum_{i=1}^{N_{\text{step}}} U_{\mathbf{k}}(t_i, t_f) f(\mathbf{k}, t_i), \tag{6b}$$

where N_{step} is the number of propagation steps and the time-evolution factor,

$$U_{\mathbf{k}}(t_i, t_f) = e^{-i\int_{t_i}^{t_f}\left[\frac{\mathbf{k}^2}{2}+\mathbf{A}(\tau)\cdot\mathbf{k}\right]d\tau}, \tag{6c}$$

is expressed in terms of the Volkov phase of the photoelectrons accumulated from t_i to t_f. Finally, the ionization probability distributions are obtained as

$$P(\mathbf{k}) = |f(\mathbf{k})|^2. \tag{6d}$$

III. THEORY

A. Perturbative treatment of the ionization amplitudes on the top of the Rabi model

In our perturbative calculations, we employ the length gauge to describe the atom-field interaction term,

$$H_{\text{int}}^{\text{L}}(t;\tau) = \mathbf{E}(t;\tau)\cdot\mathbf{r}, \tag{7}$$

where the external electric field $\mathbf{E}(t;\tau) := -d\mathbf{A}(t;\tau)/dt$ contains the two contributions from the IR and XUV fields, i.e., $\mathbf{E}(t;\tau) = \mathbf{E}_{\text{IR}}(t;\tau) + \mathbf{E}_{\text{XUV}}(t)$. To describe the physical process in the Rabi-RABBITT scheme, we preferentially deal with the Rabi oscillations within the two-level Rabi subspace $\mathcal{R} = \{|\psi_{2s}\rangle, |\psi_{2p}\rangle\}$, followed by a perturbative treatment of the transitions from Rabi subspace $\mathcal{R}$ to its orthogonal complement $\mathcal{S}$ in Hilbert space $\mathcal{H} = \mathcal{R}\bigoplus\mathcal{S}$. In doing so, the full Hamiltonian in $\mathcal{H}$ space is repartitioned as

$$H := H_0 + H_{\text{int}}^{\text{L}}(t;\tau) = H_{\mathcal{R}}(t) + H_{\text{int}}^{\perp\mathcal{R}}(t;\tau). \tag{8}$$

Here the unperturbed Hamiltonian $H_{\mathcal{R}}$ governs both Rabi dynamics within $\mathcal{R}$ subspace and the field-free evolution dynamics within $\mathcal{S}$ subspace and it is written as

$$H_{\mathcal{R}} := RH_0R + H_{\text{int}}^{\mathcal{R}}(t;\tau) + SH_0S, \tag{9}$$

where $R := |\psi_{2s}\rangle\langle\psi_{2s}| + |\psi_{2p}\rangle\langle\psi_{2p}|$ and $S := 1 - R$ are the two projectors corresponding to $\mathcal{R}$ and $\mathcal{S}$ subspaces, respectively. The interaction term $H_{\text{int}}^{\mathcal{R}}(t;\tau)$ in the Rabi Hamiltonian $H_{\mathcal{R}}$ only contains the two rotating-wave terms related to the excitation and stimulated emission processes induced by the IR field within Rabi subspace $\mathcal{R}$ and it reads

$$\begin{aligned}H_{\text{int}}^{\mathcal{R}}(t;\tau) &= \tfrac{1}{2}E_\omega \Lambda_{\text{IR}}^{\text{E}}(t;\tau)\\ &\quad\times [e^{-i\omega(t-\tau)}|\psi_{2p}\rangle\langle\psi_{2p}|(\hat{\epsilon}_{\text{IR}}\cdot\mathbf{r})|\psi_{2s}\rangle\langle\psi_{2s}|\\ &\quad+ e^{i\omega(t-\tau)}|\psi_{2s}\rangle\langle\psi_{2s}|(\hat{\epsilon}_{\text{IR}}\cdot\mathbf{r})|\psi_{2p}\rangle\langle\psi_{2p}|],\end{aligned} \tag{10}$$

where E_ω and $\Lambda_{\text{IR}}^{\text{E}}(t;\tau)$ are the amplitude and the envelope of the IR electric field, respectively. The polarization vector of the IR field is denoted as $\hat{\epsilon}_{\text{IR}}$. The interaction term $H_{\text{int}}^{\perp\mathcal{R}}(t;\tau)$ of the full Hamiltonian H in Eq. (8) is treated as a perturbation to the ongoing Rabi oscillations within $\mathcal{R}$ subspace. Using the projection operators R and S, it can be further separated as

$$\begin{aligned}H_{\text{int}}^{\perp\mathcal{R}}(t;\tau) &:= H_{\text{int}}^{\text{L}}(t;\tau) - H_{\text{int}}^{\mathcal{R}}(t;\tau)\\ &= \left[RH_{\text{int}}^{\text{L}}(t;\tau)R - H_{\text{int}}^{\mathcal{R}}(t;\tau)\right] + SH_{\text{int}}^{\text{L}}(t;\tau)S\\ &\quad+ \left[RH_{\text{int}}^{\text{L}}(t;\tau)S + SH_{\text{int}}^{\text{L}}(t;\tau)R\right],\end{aligned} \tag{11}$$

where the role of $H_{\text{int}}^{\perp\mathcal{R}}$ has three aspects: within $\mathcal{R}$, $H_{\text{int}}^{\perp\mathcal{R}}$ is responsible for the two counter-rotating-wave transitions induced by the IR field, and all possible nonresonant transitions induced by the XUV field; within $\mathcal{S}$, $H_{\text{int}}^{\perp\mathcal{R}}$ is responsible for all possible transitions induced by both the IR and XUV fields; crossing between $\mathcal{R}$ and $\mathcal{S}$, $H_{\text{int}}^{\perp\mathcal{R}}$ is responsible for all the possible transitions induced by both the IR and XUV fields.

According to the Rabi model [1], the Rabi oscillations within $\mathcal{R}$ subspace is described by the two-level wave function as

$$|\Psi_{\mathcal{R}}(t)\rangle = C_{2s}(t;\tau)e^{-i\omega_{2s}t}|\psi_{2s}\rangle + C_{2p}(t;\tau)e^{-i\omega_{2p}t}|\psi_{2p}\rangle, \tag{12}$$

where $H_0|\psi_{2s,2p}\rangle = \omega_{2s,2p}|\psi_{2s,2p}\rangle$ with ω_{2s} and ω_{2p} the energies of the $2s$ and $2p$ states. Within the subspace $\mathcal{R}$, the wave function $\Psi_{\mathcal{R}}$ obeys the Schrödinger equation governed by $H_{\mathcal{R}}$, i.e., $i\frac{d}{dt}|\Psi_{\mathcal{R}}(t)\rangle = H_{\mathcal{R}}|\Psi_{\mathcal{R}}(t)\rangle$. Symbolically, the propagator $U_{\mathcal{R}}$ corresponding to $H_{\mathcal{R}}$ is defined as

$$|\Psi_{\mathcal{R}}(t)\rangle := U_{\mathcal{R}}(t, t_0)|\Psi_{\mathcal{R}}(t_0)\rangle. \tag{13}$$

Considering that the system is initially in the $2s$ state at time t_0, i.e., $|\Psi_{\mathcal{R}}(t_0)\rangle = e^{-i\omega_{2s}t_0}|\psi_{2s}\rangle$, the time-dependent coefficients in Eq. (12) are solved as (see Appendix A)

$$\begin{aligned}C_{2s}(t;\tau) &= \cos\left[\frac{1}{2}\int_{t_0}^{t}\Omega_{\text{R}}(t';\tau)dt'\right],\\ C_{2p}(t;\tau) &= -ie^{i\omega\tau}\sin\left[\frac{1}{2}\int_{t_0}^{t}\Omega_{\text{R}}(t';\tau)dt'\right],\end{aligned} \tag{14}$$

where $\Omega_{\text{R}}(t;\tau) = \Omega_{\text{R}}^0\Lambda_{\text{IR}}^{\text{E}}(t;\tau)$ is the instantaneous Rabi frequency with its maximum value of $\Omega_{\text{R}}^0 = E_\omega\langle\psi_{2p}|(\hat{\epsilon}_{\text{IR}}\cdot\mathbf{r})|\psi_{2s}\rangle$. The factor $e^{i\omega\tau}$ in Eq. (14) comes from the time-delayed IR field. Here and hereafter the initial time for the evolution of the system is taken from minus infinity $t_0 \to -\infty$.

In the Rabi-RABBITT scheme, assuming $H_{\text{int}}^{\mathcal{R}}(t_0;\tau) = 0$ and $H_{\text{int}}^{\text{L}}(t_0;\tau) = 0$, the system is initially in the $2s$ state within $\mathcal{R}$ subspace at time t_0 and thus the initial wave function of Hilbert space $\mathcal{H}$ is $\Psi(t_0) = \Psi_{\mathcal{R}}(t_0) = e^{-i\omega_{2s}t_0}|\psi_{2s}\rangle$. Then the wave function $\Psi(t)$ describing the dynamics of the system at time t in $\mathcal{H}$ space can be written in the form of the Dyson series as [12] (see Appendix B)

$$\begin{aligned}|\Psi(t)\rangle &:= U(t, t_0)|\Psi(t_0)\rangle\\ &= U_{\mathcal{R}}(t, t_0)|\Psi(t_0)\rangle\\ &\quad- i\int_{t_0}^{t}dt_1 U(t, t_1)H_{\text{int}}^{\perp\mathcal{R}}(t_1)U_{\mathcal{R}}(t_1, t_0)|\Psi(t_0)\rangle\\ &= |\Psi_{\mathcal{R}}(t)\rangle - i\int_{t_0}^{t}dt_1 U(t, t_1)H_{\text{int}}^{\perp\mathcal{R}}(t_1)|\Psi_{\mathcal{R}}(t_1)\rangle,\end{aligned} \tag{15}$$

where U is the propagator related to the full Hamiltonian H. In the last line of Eq. (15), the first term describes the unperturbed Rabi oscillations within the two-level subspace $\mathcal{R}$; and the second term describes the transition from the Rabi wave function $\Psi_{\mathcal{R}}$ of the subspace $\mathcal{R}$ outwards to its orthogonal complement $\mathcal{S}$ through the interaction $H_{\text{int}}^{\perp\mathcal{R}}$ followed by its full propagation under H, which contains the ionization part of the wave function.

According to Eq. (8), the full propagator $U(t,t_1)$ can be alternatively written as

$$U(t,t_1)=U_0(t,t_1)-i\int_{t_1}^{t}dt_2U(t,t_2)H_{\text{int}}^{\text{L}}(t_2)U_0(t_2,t_1) \quad (16)$$

where U_0 is the propagator related to the field-free Hamiltonian H_0. Here $U_0(t,t')$ can be expanded on the eigenstates of H_0 as $U_0(t,t')=\sum_{\nu}|\psi_\nu\rangle\langle\psi_\nu|\exp[-i\omega_\nu(t-t')]$ with $H_0|\psi_n\rangle=\omega_n|\psi_n\rangle$. Substituting Eq. (16) into Eq. (15), the wave function can be expanded iteratively to arbitrary order in the interaction term as

$$|\Psi(t)\rangle=\sum_{N=0}^{\infty}|\bar{\Psi}^{(N)}(t)\rangle, \quad (17)$$

where the zeroth-order wave packet is the Rabi wave function $|\bar{\Psi}^{(0)}(t)\rangle=|\Psi_{\mathcal{R}}(t)\rangle$ in Eq. (12) and where the first-order wave packet is $|\bar{\Psi}^{(1)}(t)\rangle=-i\int_{t_0}^{t}dt_1U_0(t,t_1)H_{\text{int}}^{\perp\mathcal{R}}(t_1)|\Psi_{\mathcal{R}}(t_1)\rangle$, which describes the transition from the Rabi wave function $\Psi_{\mathcal{R}}$ through the first-order interaction $H_{\text{int}}^{\perp\mathcal{R}}$. Likewise, for the wave packets to higher orders $N>1$, $|\Psi^{(N)}(t)\rangle$ originates from the Nth-order interaction and it is derived from Eq. (15) as

$$\begin{aligned}|\bar{\Psi}^{(N>1)}(t)\rangle=&(-i)^N\int_{t_0}^{t}dt_1\int_{t_1}^{t}dt_2\cdots\int_{t_{N-1}}^{t}dt_N\\&\times U_0(t,t_N)H_{\text{int}}^{\text{L}}(t_N)U_0(t_N,t_{N-1})H_{\text{int}}^{\text{L}}(t_{N-1})\times\cdots\\&\times H_{\text{int}}^{\text{L}}(t_2)U_0(t_2,t_1)H_{\text{int}}^{\perp\mathcal{R}}(t_1)|\Psi_{\mathcal{R}}(t_1)\rangle, \quad (18)\end{aligned}$$

with the time order $t>t_N>t_{N-1}>\cdots>t_2>t_1>t_0$. Here in our perturbative treatment of the ionization process on the top of the Rabi model, we assume the ongoing Rabi oscillations with $\mathcal{R}$ are perfect: the energy shifts of the $2s$ and $2p$ states, the population leakage to $\mathcal{S}$ subspace, and the dampening in Rabi oscillations are all negligible. Moreover, we assume the timescale of the process we are investigating is much shorter than the lifetime of the $2s$ and $2p$ states.

The Nth-order transition amplitude $a_f^{(N)}$ is obtained by projecting the Nth-order wave function $|\Psi^{(N)}(t)\rangle$ to the final state $|\phi_f\rangle$ of a specific energy ω_f as [62]

$$a_f^{(N)}=\lim_{t\to\infty}\langle\phi_f(t)|\Psi^{(N)}(t)\rangle, \quad (19)$$

where $|\phi_f(t)\rangle=e^{-i\omega_f t}|\psi_f\rangle$, with $|\psi_f\rangle$ satisfying $H_0|\psi_f\rangle=\omega_f|\psi_f\rangle$. Here we take $t\to\infty$ because the photoelectrons are measured long after the interaction with the field is over. In the case of $\omega_f>0$, $a_f^{(N>0)}$ represents the N-photon ionization amplitude from the Rabi wave function $\Psi_{\mathcal{R}}$ with all possible combinations of photons in different time orders. To further specify different ionization processes in the total Nth-order transition amplitude $a_f^{(N)}$, the interaction terms $H_{\text{int}}^{\text{L}}$ and $H_{\text{int}}^{\perp\mathcal{R}}$ are separated into different laser components in Eq. (18). For example, the interaction term is $E_{\text{IR}}(t;\tau)\hat{O}_\omega$ for the IR photon and it is $E_{\Omega_{2q+1}}(t)\hat{O}_\Omega$ for the XUV harmonics of the frequency $\Omega_{2q+1}=(2q+1)\omega$, which contain both absorption and emission terms. Here the transition operators are written in the length gauge as $\hat{O}_\omega:=\hat{\epsilon}_{\text{IR}}\cdot\mathbf{r}$ and $\hat{O}_\Omega:=\hat{\epsilon}_{\text{XUV}}\cdot\mathbf{r}$, with $\hat{\epsilon}_{\text{XUV}}$ the polarization vector of the XUV field, assuming all XUV harmonics have the same polarization. In particular, when considering the XUV, XUV + IR, and XUV + IR + IR absorption processes, the corresponding ionization amplitudes are derived as

$$\begin{aligned}a_{\text{XUV}}^{(1)}=&-i\int_{-\infty}^{\infty}d\omega_{\text{R}}\tilde{C}_{2s}(\omega_{\text{R}};\tau)\tilde{E}_{\Omega_{2q+1}}(\omega_f-\omega_{2s}-\omega_{\text{R}})\langle\psi_f|\hat{O}_\Omega|\psi_{2s}\rangle-i\int_{-\infty}^{\infty}d\omega_{\text{R}}\tilde{C}_{2p}(\omega_{\text{R}};\tau)\\&\times\tilde{E}_{\Omega_{2q+1}}(\omega_f-\omega_{2p}-\omega_{\text{R}})\langle\psi_f|\hat{O}_\Omega|\psi_{2p}\rangle, \quad (20\text{a})\end{aligned}$$

$$\begin{aligned}a_{\text{XUV+IR}}^{(2)}=&-\frac{i}{\sqrt{2\pi}}\int_{-\infty}^{\infty}d\omega_{\text{R}}\tilde{C}_{2s}(\omega_{\text{R}};\tau)\int_0^{\infty}d\Omega e^{i(\omega_f-\Omega-\omega_{2s}-\omega_{\text{R}})\tau}\tilde{E}_{\text{IR}}(\omega_f-\Omega-\omega_{2s}-\omega_{\text{R}})\tilde{E}_{\Omega_{2q+1}}(\Omega)\\&\times\sum_{\nu_1}\frac{\langle\psi_f|\hat{O}_\omega|\psi_{\nu_1}\rangle\langle\psi_{\nu_1}|\hat{O}_\Omega|\psi_{2s}\rangle}{\omega_{2s}+\omega_{\text{R}}+\Omega-\omega_{\nu_1}}-\frac{i}{\sqrt{2\pi}}\int_{-\infty}^{\infty}d\omega_{\text{R}}\tilde{C}_{2p}(\omega_{\text{R}};\tau)\int_0^{\infty}d\Omega e^{i(\omega_f-\Omega-\omega_{2p}-\omega_{\text{R}})\tau}\\&\times\tilde{E}_{\text{IR}}(\omega_f-\Omega-\omega_{2p}-\omega_{\text{R}})\tilde{E}_{\Omega_{2q+1}}(\Omega)\sum_{\nu_1}\frac{\langle\psi_f|\hat{O}_\omega|\psi_{\nu_1}\rangle\langle\psi_{\nu_1}|\hat{O}_\Omega|\psi_{2p}\rangle}{\omega_{2p}+\omega_{\text{R}}+\Omega-\omega_{\nu_1}}, \quad (20\text{b})\end{aligned}$$

$$\begin{aligned}a_{\text{XUV+IR+IR}}^{(3)}=&-\frac{i}{2\pi}\int_{-\infty}^{\infty}d\omega_{\text{R}}\tilde{C}_{2s}(\omega_{\text{R}};\tau)\int_0^{\infty}d\omega\int_0^{\infty}d\Omega e^{i(\omega_f-\Omega-\omega_{2s}-\omega_{\text{R}})\tau}\tilde{E}_{\text{IR}}(\omega_f-\omega-\Omega-\omega_{2s}-\omega_{\text{R}})\tilde{E}_{\text{IR}}(\omega)\tilde{E}_{\Omega_{2q+1}}(\Omega)\\&\times\sum_{\nu_1,\nu_2}\frac{\langle\psi_f|\hat{O}_\omega|\psi_{\nu_2}\rangle\langle\psi_{\nu_2}|\hat{O}_\omega|\psi_{\nu_1}\rangle\langle\psi_{\nu_1}|\hat{O}_\Omega|\psi_{2s}\rangle}{(\omega_{2s}+\omega_{\text{R}}+\Omega+\omega-\omega_{\nu_2})(\omega_{2s}+\omega_{\text{R}}+\Omega-\omega_{\nu_1})}-\frac{i}{2\pi}\int_{-\infty}^{\infty}d\omega_{\text{R}}\tilde{C}_{2p}(\omega_{\text{R}};\tau)\int_0^{\infty}d\omega\\&\times\int_0^{\infty}d\Omega e^{i(\omega_f-\Omega-\omega_{2p}-\omega_{\text{R}})\tau}\tilde{E}_{\text{IR}}(\omega_f-\omega-\Omega-\omega_{2p}-\omega_{\text{R}})\tilde{E}_{\text{IR}}(\omega)\tilde{E}_{\Omega_{2q+1}}(\Omega)\\&\times\sum_{\nu_1,\nu_2}\frac{\langle\psi_f|\hat{O}_\omega|\psi_{\nu_2}\rangle\langle\psi_{\nu_2}|\hat{O}_\omega|\psi_{\nu_1}\rangle\langle\psi_{\nu_1}|\hat{O}_\Omega|\psi_{2p}\rangle}{(\omega_{2p}+\omega_{\text{R}}+\Omega+\omega-\omega_{\nu_2})(\omega_{2p}+\omega_{\text{R}}+\Omega-\omega_{\nu_1})}, \quad (20\text{c})\end{aligned}$$

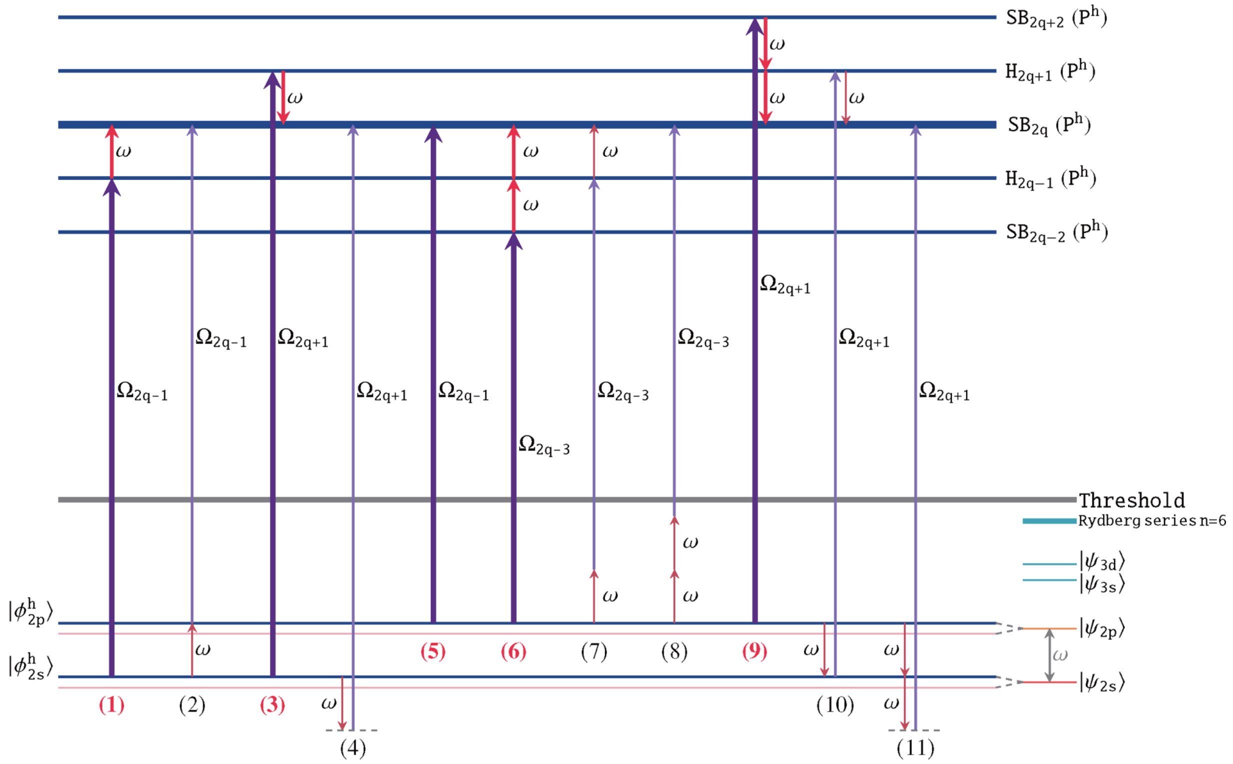

FIG. 2. The schematic of ionization pathways for $\mathrm{P^h}$ with the photoelectron energy of $2q\omega - I_p^{2s} + \omega_\mathrm{R}$ ($\omega_\mathrm{R} \approx \Omega_\mathrm{R}^0/2$). The purple and red arrows indicate the transition by exchanging the XUV and IR photons, respectively. The essential pathways are drawn in thick-line arrows. The less-contributed pathways are represented by thin-line arrows.

where ν_i identifies the intermediate unperturbed states $|\psi_{\nu_i}\rangle$ of the energy ω_{ν_i} as $H_0|\psi_{\nu_i}\rangle = \omega_{\nu_i}|\psi_{\nu_i}\rangle$; ω and Ω are the frequencies of the IR photon and the $(2q+1)$th-order XUV harmonics, respectively. Here, we use the relation of the delta function $\delta(\omega) = \int_{-\infty}^{\infty} e^{i\omega t}dt/(2\pi)$ and the Fourier transform (FT): $\tilde{f}(\omega) = \frac{1}{\sqrt{2\pi}}\int_{-\infty}^{\infty} f(t)e^{i\omega t}dt$, $f(t) = \frac{1}{\sqrt{2\pi}}\int_{-\infty}^{\infty} \tilde{f}(\omega)e^{-i\omega t}d\omega$, and $\tilde{f}(\omega;\tau) := \frac{1}{\sqrt{2\pi}}\int_{-\infty}^{\infty} f(t;\tau)e^{i\omega t}dt = \tilde{f}(\omega)e^{i\omega\tau}$. The FT of the Rabi amplitudes [Eq. (14)] are $\tilde{C}_{2s,2p}(\omega_\mathrm{R};\tau) := \frac{1}{\sqrt{2\pi}}\int_{-\infty}^{\infty} C_{2s,2p}(t;\tau)e^{-i\omega_\mathrm{R}t}d\omega_\mathrm{R} = \tilde{C}_{2s,2p}(\omega_\mathrm{R})e^{i\omega_\mathrm{R}\tau}$ (see Appendix A), where ω_R is the frequency component of the Rabi amplitudes. For the long IR field of flat-top envelope [Eq. (3b)], the Rabi amplitudes mainly distribute at $\omega_\mathrm{R} \approx \pm\Omega_\mathrm{R}^0/2$ in the frequency domain. Equation (20a) describes the one-photon transition from the zeroth-order Rabi wave function $|\Psi_\mathcal{R}\rangle$ to the continuum state $|\phi_f\rangle$ by absorbing an XUV photon of the frequency $\Omega = \omega_f - \omega_{2s,2p} - \omega_\mathrm{R}$; Eq. (20b) describes the two-photon transition through the absorption of an XUV photon followed by the absorption of an IR photon, where the energy-preserving condition $\omega_f = \omega_{2s,2p} + \omega_\mathrm{R} + \Omega + \omega$ is satisfied; and Eq. (20c) describes the three-photon transition through the absorption of an XUV photon followed by the absorption of two IR photons, where the energy-preserving condition $\omega_f = \omega_{2s,2p} + \omega_\mathrm{R} + \Omega + 2\omega$ is satisfied.

As indicated by the term ω_R in the denominators in Eqs. (20), the ionization from the Rabi state $|\Psi_\mathcal{R}\rangle$ can be understood to start from the dressed states of $|\psi_{2s}\rangle$ and $|\psi_{2p}\rangle$, which spilt into two quasienergies considering the sign of ω_R. More specifically, the first (second) term in Eqs. (20) corresponds to the ionization from the dressed $2s$ ($2p$) states with the quasienergies of $\omega_{2s} + \omega_\mathrm{R}$ ($\omega_{2p} + \omega_\mathrm{R}$), where $\omega_\mathrm{R} \approx -\Omega_\mathrm{R}^0/2$ for $|\phi^{l}_{2s}\rangle$ ($|\phi^{l}_{2p}\rangle$) and $\omega_\mathrm{R} \approx \Omega_\mathrm{R}^0/2$ for $|\phi^{h}_{2s}\rangle$ ($|\phi^{h}_{2p}\rangle$), respectively. In the photoelectron spectra, the peak of a lower (higher) photoelectron energy in the AT doublet, namely, $\mathrm{P^l}$ ($\mathrm{P^h}$), is formed by the interference among all the ionization pathways initiated from $|\phi^{l}_{2s}\rangle$ and $|\phi^{l}_{2p}\rangle$ ($|\phi^{h}_{2s}\rangle$ and $|\phi^{h}_{2p}\rangle$).

B. Ionization pathways

As an example, we display the ionization pathways contributing to $\mathrm{P^h}$ with the photoelectron energy of $2q\omega - I_p^{2s} + \omega_\mathrm{R}$ ($\omega_\mathrm{R} \approx \Omega_\mathrm{R}^0/2$) in Fig. 2. Pathways 1 to 4 are initiated from $|\phi^{h}_{2s}\rangle$, among which pathways 1 and 3 are reminiscent of the well-known two-photon transitions in the traditional RABBITT cases [63]. Pathways 1 and 2 denote the absorption of one $(2q-1)$st-order XUV harmonic Ω_{2q-1} and one IR photon ω in different time orders. Note that, as indicated by the term $H_\mathrm{int}^{\perp\mathcal{R}}$ in Eq. (18), ψ_{2p} needs to be excluded from the intermediate summation in calculating the transition amplitude of pathway 2 since this transition has been handled in the nonperturbative treatment of the Rabi oscillations. Pathways 3 and 4 denote the absorption of one $(2q+1)$st-order XUV harmonic Ω_{2q+1} and the emission of one IR photon ω in different time orders. In our case, because the $2p$ state is also populated during Rabi oscillations, there are also pathways initiated from $|\phi^{h}_{2p}\rangle$, as denoted by pathways 5 to 11 in Fig. 2. Pathway 5 indicates the absorption of one $(2q-1)$st-order XUV harmonic Ω_{2q-1}. Pathways 6 to 8 refer to the absorption of one $(2q-3)$rd-order XUV harmonic Ω_{2q-3} and two IR photons in different time orders. Pathways 9 to 11 denote the absorption of one XUV photon $\Omega_{\mathrm{2q+1}}$ and the emission of two IR photons in different time orders. Similarly as pathway 2, in calculating the transition amplitude of pathways 10 and 11, ψ_{2s} needs to be excluded from the first intermediate summation. Pathways of essential contribution are pathways 1, 3, 5, 6, and 9, whose numbers are highlighted in red in Fig. 2.

In our calculations, the XUV and flat-top IR fields are both spectrally narrow enough and display no spectral overlap. Therefore, the convolution can be reasonably dismissed and both laser fields are approximated as monochromatic: let $E_{\mathrm{IR}}(t;\tau) = E_\omega \cos[\omega(t-\tau)]$ and $E_{\Omega_{\mathrm{2q+1}}}(t) = E_{\mathrm{2q+1}} \cos(\Omega_{\mathrm{2q+1}}t - \phi_{\mathrm{2q+1}})$, with the amplitude $E_{\mathrm{2q+1}}$ and the phase $\phi_{\mathrm{2q+1}}$ associated with the $(2q+1)$st-order XUV harmonic; and let $\tilde{C}_{2s}(\omega_{\mathrm{R}};\tau) = \sqrt{\pi/2}e^{i\omega_{\mathrm{R}}\tau}[\delta(\omega_{\mathrm{R}} + |\Omega_{\mathrm{R}}^0|/2) + \delta(\omega_{\mathrm{R}} - |\Omega_{\mathrm{R}}^0|/2)]$ and $\tilde{C}_{2p}(\omega_{\mathrm{R}};\tau) = -\sqrt{\pi/2}\frac{\Omega_{\mathrm{R}}^0}{|\Omega_{\mathrm{R}}^0|}e^{i(\omega+\omega_{\mathrm{R}})\tau}[\delta(\omega_{\mathrm{R}} + |\Omega_{\mathrm{R}}^0|/2) - \delta(\omega_{\mathrm{R}} - |\Omega_{\mathrm{R}}^0|/2)]$. Then each term in Eqs. (20) can be approximately calculated by multiplying the corresponding IR (E_ω) and XUV ($E_{\mathrm{2q+1}}$) electric-field amplitudes to the residual integration of wave functions. For example, the ionization amplitudes $\mathcal{A}_{\mathcal{P}}$ for SB_{2q}, where $\mathcal{P}$ characterizes the specific pathway, i.e., $\mathcal{P} \in \{\text{pathway } (i) | i = 1, \ldots, 11\}$, are given as (see Appendix C for the other pathways)

$$\mathcal{A}_{(1)}(\vec{k}_\pm,\tau) = -\frac{i\pi}{4}e^{i[(\omega\pm\frac{|\Omega_{\mathrm{R}}^0|}{2})\tau+\phi_{2q-1}]}E_\omega E_{\mathrm{2q-1}}\sum_{\nu_1}\frac{\langle\psi_{f\pm}|\hat{O}_\omega|\psi_{\nu_1}\rangle\langle\psi_{\nu_1}|\hat{O}_\Omega|\psi_{2s}\rangle}{\omega_{2s}\pm\frac{|\Omega_{\mathrm{R}}^0|}{2}+\Omega_{2q-1}-\omega_{\nu_1}}, \tag{21a}$$

$$\mathcal{A}_{(3)}(\vec{k}_\pm,\tau) = -\frac{i\pi}{4}e^{-i[(\omega\mp\frac{|\Omega_{\mathrm{R}}^0|}{2})\tau-\phi_{2q+1}]}E_\omega E_{\mathrm{2q+1}}\sum_{\nu_1}\frac{\langle\psi_{f\pm}|\hat{O}_\omega^\dagger|\psi_{\nu_1}\rangle\langle\psi_{\nu_1}|\hat{O}_\Omega|\psi_{2s}\rangle}{\omega_{2s}\pm\frac{|\Omega_{\mathrm{R}}^0|}{2}+\Omega_{2q+1}-\omega_{\nu_1}}, \tag{21b}$$

$$\mathcal{A}_{(5)}(\vec{k}_\pm,\tau) = \mp\frac{i\pi\Omega_{\mathrm{R}}^0}{2|\Omega_{\mathrm{R}}^0|}e^{i[(\omega\pm\frac{|\Omega_{\mathrm{R}}^0|}{2})\tau+\phi_{2q-1}]}E_{\mathrm{2q-1}}\langle\psi_{f\pm}|\hat{O}_\Omega|\psi_{2p}\rangle, \tag{21c}$$

$$\mathcal{A}_{(6)}(\vec{k}_\pm,\tau) = \mp\frac{i\pi\Omega_{\mathrm{R}}^0}{8|\Omega_{\mathrm{R}}^0|}e^{i[(3\omega\pm\frac{|\Omega_{\mathrm{R}}^0|}{2})\tau+\phi_{2q-3}]}E_\omega^2 E_{\mathrm{2q-3}}\sum_{\nu_1,\nu_2}\frac{\langle\psi_{f\pm}|\hat{O}_\omega|\psi_{\nu_2}\rangle\langle\psi_{\nu_2}|\hat{O}_\omega|\psi_{\nu_1}\rangle\langle\psi_{\nu_1}|\hat{O}_\Omega|\psi_{2p}\rangle}{\left(\omega_{2p}\pm\frac{|\Omega_{\mathrm{R}}^0|}{2}+\Omega_{2q-3}+\omega-\omega_{\nu_2}\right)\left(\omega_{2p}\pm\frac{|\Omega_{\mathrm{R}}^0|}{2}+\Omega_{2q-3}-\omega_{\nu_1}\right)}, \tag{21d}$$

$$\mathcal{A}_{(9)}(\vec{k}_\pm,\tau) = \mp\frac{i\pi\Omega_{\mathrm{R}}^0}{8|\Omega_{\mathrm{R}}^0|}e^{-i[(\omega\mp\frac{|\Omega_{\mathrm{R}}^0|}{2})\tau-\phi_{2q+1}]}E_\omega^2 E_{\mathrm{2q+1}}$$

$$\times\sum_{\nu_1,\nu_2}\frac{\langle\psi_{f\pm}|\hat{O}_\omega^\dagger|\psi_{\nu_2}\rangle\langle\psi_{\nu_2}|\hat{O}_\omega^\dagger|\psi_{\nu_1}\rangle\langle\psi_{\nu_1}|\hat{O}_\Omega|\psi_{2p}\rangle}{\left(\omega_{2p}\pm\frac{|\Omega_{\mathrm{R}}^0|}{2}+\Omega_{2q+1}-\omega-\omega_{\nu_2}\right)\left(\omega_{2p}\pm\frac{|\Omega_{\mathrm{R}}^0|}{2}+\Omega_{2q+1}-\omega_{\nu_1}\right)}, \tag{21e}$$

where ψ_{f+} (ψ_{f-}) is the final continuum state related to the peak $\mathrm{P^h}$ ($\mathrm{P^l}$) of the AT doublet. The energy and the asymptotic momentum of $\psi_{f\pm}$ are $E_\pm = 2q\omega - I_p^{2s} \pm \frac{|\Omega_{\mathrm{R}}^0|}{2} = k_\pm^2/2$ and $\vec{k}_\pm := k_\pm\hat{k}_\pm$, respectively. Here, as indicated by Eqs. (12) and (14), the zeroth-order Rabi wave function $\Psi_{\mathcal{R}}$ evolving with the time-delayed IR field leads to the factors $\exp[\pm i(|\Omega_{\mathrm{R}}^0|/2)\tau]$ and $\exp[i(\omega \pm |\Omega_{\mathrm{R}}^0|/2)\tau]$ in Eqs. (21), respectively for the ionization pathways from the $2s$ and $2p$ states. In addition, the initial phase of the electron wave packet generated from $|\phi_{2p}^{\mathrm{l}}\rangle$ has an additional term of π compared with that for $|\phi_{2p}^{\mathrm{h}}\rangle$, as implied by the beginning sign $\mp$ of the ionization amplitudes for pathways 5 to 11. These different initial phases between the dressed $2p$ states stem from the sine-like Rabi amplitude of the $2p$ state, as indicated by Eq. (14).

In calculation, the incoming final continuum state $\psi_{\vec{k}_\pm}^-(\vec{r}\,) := \langle\vec{r}\,|\psi_{f\pm}\rangle$ [64,65] can be further expanded on the partial wave series as [66]

$$\psi_{\vec{k}_\pm}^-(\vec{r}\,) = \frac{1}{k_\pm^{1/2}}\sum_{L=0}^{\infty}\sum_{M=-L}^{L} i^L e^{-i(\sigma_{L\pm}+\delta_{L\pm})} \times Y_{L,M}^*(\hat{k}_\pm)R_{E_\pm,L}(r)Y_{L,M}(\hat{r}), \tag{22}$$

where L and M are the angular-momentum quantum number and the magnetic quantum number of the partial wave, respectively. Here the phase shift due to the short-range potential is $\delta_{L\pm}$ in lithium atom [56]. The Coulombic phase is $\sigma_{L\pm} := \arg[\Gamma(1 + L - iZ/k_\pm)]$ with the effective nuclear charge $Z = 1$. The energy-normalized radial wave function is $R_{E_\pm L}(r)$ with its asymptotic behavior of $\sqrt{2/(\pi k_\pm r)}\sin[k_\pm r - L\pi/2 - Z\ln(2k_\pm r)/k_\pm + \sigma_{L\pm} + \delta_{L\pm}]$ when $r \to \infty$.

C. The Rabi-RABBITT scheme using circularly polarized laser fields

In the traditional RABBITT scheme with linearly polarized XUV and IR fields [63], absorbing (emitting) an IR photon from the retarded ($\tau > 0$) IR field $\mathbf{E}_{\mathrm{IR}}(t - \tau)$ with respect to the XUV field $\mathbf{E}_{\mathrm{XUV}}(t)$ contributes a phase like $e^{+i\omega\tau}$ ($e^{-i\omega\tau}$) with $\omega > 0$[1]. Therefore, the number of exchanged IR photons in each ionization pathway is imprinted in the τ-related phase of the outgoing electron wave packet. Thus, the relative phase

---

[1] Alternatively, absorbing an XUV photon from the XUV field $\mathbf{E}_{\mathrm{XUV}}(t + \tau)$ in advance of the IR field $\mathbf{E}_{\mathrm{IR}}(t)$ corresponds to an interaction phase of $e^{-i\Omega_{\mathrm{2q+1}}\tau}$ with $\Omega_{\mathrm{2q+1}} > 0$. The equivalence of these two perspectives is established upon the energy-preserving condition during the ionization process.

TABLE II. The magnetic quantum number of the final continuum state (M) for pathways 1 to 11 (denoted as P1 to P11), the oscillation components in SBs as a function of azimuthal angle φ, and the phase matching situation in experiments, under nine combinations of the laser field polarizations (denoted as Cases 1 to 9). The polarization of the fields is characterized by the dipole selection rules for the magnetic quantum number (Δm): $\Delta m = 0$, $\Delta m = +1$, and $\Delta m = -1$ denote the linearly, left-hand circularly, and right-hand circularly polarized fields, respectively.

Case	XUV field	IR field	P1	P2	P3	P4	P5	P6	P7	P8	P9	P10	P11	φ oscillations	Phase matched
1	$\Delta m = +1$	$\Delta m = +1$	2	2	0	0	2	4	4	4	0	0	0	$2\varphi, 4\varphi$	Yes
2	$\Delta m = +1$	$\Delta m = -1$	0	0	2	2	0	−2	−2	−2	2	2	2	$2\varphi, 4\varphi$	Yes
3	$\Delta m = -1$	$\Delta m = +1$	0	0	−2	−2	0	2	2	2	−2	−2	−2	$2\varphi, 4\varphi$	Yes
4	$\Delta m = -1$	$\Delta m = -1$	−2	−2	0	0	−2	−4	−4	−4	0	0	0	$2\varphi, 4\varphi$	Yes
5	$\Delta m = 0$	$\Delta m = +1$	1	1	−1	−1	1	3	3	3	−1	−1	−1	$2\varphi, 4\varphi$	No
6	$\Delta m = 0$	$\Delta m = -1$	−1	−1	1	1	−1	−3	−3	−3	1	1	1	$2\varphi, 4\varphi$	No
7	$\Delta m = +1$	$\Delta m = 0$	1	1	1	1	1	1	1	1	1	1	1	No	No
8	$\Delta m = -1$	$\Delta m = 0$	−1	−1	−1	−1	−1	−1	−1	−1	−1	−1	−1	No	No
9	$\Delta m = 0$	$\Delta m = 0$	0	0	0	0	0	0	0	0	0	0	0	No	Yes

of the outgoing electron wave packets at the same energy via different pathways, named the *RABBITT phase*, can be retrieved from the $2\omega\tau$ modulation of SBs [36]. As discussed in Ref. [54], by using different combinations of the XUV and IR fields with either linear or circular polarizations[2], it is possible to extract the RABBITT phases from the modulation of SBs as a function of azimuthal angle φ. The mechanism behind this alternative way[3] to extract the RABBITT phases is based on the dipole selection rules: exchanging one circularly polarized IR photon will increase or decrease the magnetic quantum number M. Finally, the number of exchanged circularly polarized IR photons is encoded in the φ-related phase of the outgoing wave packet via $e^{iM\varphi}$ originating from $Y^*_{L,M}(\hat{k}_\pm)$ in Eq. (22).

In principle, we have nine possible combinations of the polarizations of the XUV and IR fields, as listed by Cases 1 to 9 in Table II. The corresponding transition operators $\hat{O}_\omega$ and $\hat{O}_\Omega$ used in Eqs. (21) are $r\cos\theta$, $r\sin\theta e^{i\varphi}/\sqrt{2}$, and $r\sin\theta e^{-i\varphi}/\sqrt{2}$ for linear, left-hand circular, and right-hand circular polarizations, respectively [67]. Note that phase matching is only achievable in experiments for Cases 1, 2, 3, 4, and 9. Table II gives that, *if only* the circularly polarized IR field is used (Cases 1 to 6), the RABBITT phases can be successfully extracted from the 2φ oscillations of SBs without scan of the time delay between the XUV and IR fields. In addition, Cases 1 to 6 all give the same interference scheme as using both linearly polarized XUV and IR fields (Case 9). More specifically, 2φ signal (4φ signal) results from the interference of pathways 1, 2, 5 versus 3, 4, 6, 7, 8, 9, 10, 11 (pathways 3, 4, 9, 10, 11 versus 6, 7, 8). As a demonstration, we show as follows how to extract the RABBITT phases from the 2φ oscillations in the Rabi-RABBITT scheme for *Case 1* (Sec. IV A) and *Case 2* (Sec. IV B).

Substituting Eq. (22) into Eqs. (21), the ionization amplitude of pathway i can be written as

$$\mathcal{A}_{(i)}(\vec{k}_\pm, \tau) = \sum_{\mathcal{Q}} \mathcal{A}_{(i),\mathcal{Q}}(\vec{k}_\pm, \tau). \tag{23}$$

Here $\mathcal{A}_{(i),\mathcal{Q}}$ is the amplitude of a specified ionization channel for pathway $i \in \{1, 2, \dots, 11\}$, which is unambiguously characterized by the quantum numbers throughout all the states in transition. In N-photon transition, the ensemble of these quantum numbers is defined as $\mathcal{Q} = (l_i, m_i), (\lambda_1, \mu_1), \dots, (\lambda_{N-1}, \mu_{N-1}), (L, M)$, where l_i, λ_{N-1}, and L (m_i, μ_{N-1}, and M) respectively label the angular (magnetic) quantum numbers of the initial, the $(N-1)$st intermediate, and the final states. The specific quantum numbers in $\mathcal{Q}$ are determined by the selection rules, taking *Case 1* as an example, we have $\Delta m = +1$ ($\Delta m = -1$) for absorption (emission) with $l \geqslant m$. For a single time-delay ($\tau = 0$) RABBITT measurement in *Case 1*, $\mathcal{A}_{(i),\mathcal{Q}}$ can be written as

$$\mathcal{A}_{(i),\mathcal{Q}}(\vec{k}_\pm, \tau = 0) = \frac{\pi}{k_\pm^{1/2}} Y_{L,M}(\hat{k}_\pm) \mathcal{M}_{(i),\mathcal{Q}}(E_\pm), \tag{24}$$

where $\hat{k}_\pm = (\theta, \varphi)$ indicates the emission direction of photoelectrons. The amplitudes $\mathcal{M}_{(i),\mathcal{Q}}(E_\pm)$ can be further separated into its angular and radial parts in coordinate representation as (see Appendix C for the other

---

[2] Note that in the coordinate system used here, the xOy plane is defined as the polarization plane of the circularly polarized fields; and the z axis is defined as the propagation direction of the circularly polarized fields and the polarization axis of the linearly polarized fields. This definition of the coordinate system for the circularly polarized fields differs from that used in our TDSE calculations [Eqs. (3a) and (4a)], however, the observed physical quantities are unchanged under the rotation $[\mathcal{C} : (\hat{e}_x, \hat{e}_y, \hat{e}_z) \rightarrow \mathcal{C}' : (\hat{e}_z, \hat{e}_x, \hat{e}_y)]$ of the coordinate system fixed with an observer.

[3] According to the dipole selection rules, the involved ionization channels are different in the cases of linearly and circularly polarized fields and thus the retrieved RABBITT phases are inequivalent.

pathways)

$$\mathcal{M}_{(1),\mathcal{Q}}(E_\pm) = \frac{\pi}{3} E_\omega E_{2\mathrm{q}-1} i^{-(L+1)} e^{i(\sigma_{L\pm}+\delta_{L\pm}+\phi_{2q-1})} \langle Y_{L,M}|Y_{1,1}\big|Y_{\lambda_1,\mu_1}\big\rangle\big\langle Y_{\lambda_1,\mu_1}\big|Y_{1,1}|Y_{0,0}\rangle \sum\!\!\!\!\!\!\!\int_{\nu_1} \frac{\langle R_{E_\pm,L}|r\big|R_{\nu_1,\lambda_1}\big\rangle\big\langle R_{\nu_1,\lambda_1}\big|r|R_{2,0}\rangle}{\omega_{2s} \pm \frac{|\Omega_{\mathrm{R}}^0|}{2} + \Omega_{2q-1} - \omega_{\nu_1}}, \tag{25a}$$

$$\mathcal{M}_{(3),\mathcal{Q}}(E_\pm) = -\frac{\pi}{3} E_\omega E_{2\mathrm{q}+1} i^{-(L+1)} e^{i(\sigma_{L\pm}+\delta_{L\pm}+\phi_{2q+1})} \langle Y_{L,M}|Y_{1,-1}\big|Y_{\lambda_1,\mu_1}\big\rangle\big\langle Y_{\lambda_1,\mu_1}\big|Y_{1,1}|Y_{0,0}\rangle \sum\!\!\!\!\!\!\!\int_{\nu_1} \frac{\langle R_{E_\pm,L}|r\big|R_{\nu_1,\lambda_1}\big\rangle\big\langle R_{\nu_1,\lambda_1}\big|r|R_{2,0}\rangle}{\omega_{2s} \pm \frac{|\Omega_{\mathrm{R}}^0|}{2} + \Omega_{2q+1} - \omega_{\nu_1}}, \tag{25b}$$

$$\mathcal{M}_{(5),\mathcal{Q}}(E_\pm) = -\left(\frac{\pi}{3}\right)^{\frac{1}{2}} \frac{\Omega_{\mathrm{R}}^0}{\left|\Omega_{\mathrm{R}}^0\right|} E_{2\mathrm{q}-1} i^{-(L\pm1)} e^{i(\sigma_{L\pm}+\delta_{L\pm}+\phi_{2q-1})} \langle Y_{L,M}|Y_{1,1}|Y_{1,1}\rangle \langle R_{E_\pm,L}|r|R_{2,1}\rangle, \tag{25c}$$

$$\begin{aligned} \mathcal{M}_{(6),\mathcal{Q}}(E_\pm) = {}& -\left(\frac{\pi}{3}\right)^{\frac{3}{2}} \frac{\Omega_{\mathrm{R}}^0}{\left|\Omega_{\mathrm{R}}^0\right|} E_\omega^2 E_{2\mathrm{q}-3} i^{-(L\pm1)} e^{i\left(\sigma_{L\pm}+\delta_{L\pm}+\phi_{2q-3}\right)} \langle Y_{L,M}|Y_{1,1}\big|Y_{\lambda_2,\mu_2}\big\rangle\big\langle Y_{\lambda_2,\mu_2}\big|Y_{1,1}\big|Y_{\lambda_1,\mu_1}\big\rangle\big\langle Y_{\lambda_1,\mu_1}\big|Y_{1,1}|Y_{1,1}\rangle \\ & \times \sum\!\!\!\!\!\!\!\int_{\nu_1,\nu_2} \frac{\langle R_{E_\pm,L}|r\big|R_{\nu_2,\lambda_2}\big\rangle\big\langle R_{\nu_2,\lambda_2}\big|r\big|R_{\nu_1,\lambda_1}\big\rangle\big\langle R_{\nu_1,\lambda_1}\big|r|R_{2,1}\rangle}{\left(\omega_{2p} \pm \frac{\left|\Omega_{\mathrm{R}}^0\right|}{2} + \Omega_{2q-3} + \omega - \omega_{\nu_2}\right)\left(\omega_{2p} \pm \frac{\left|\Omega_{\mathrm{R}}^0\right|}{2} + \Omega_{2q-3} - \omega_{\nu_1}\right)}, \end{aligned} \tag{25d}$$

$$\begin{aligned} \mathcal{M}_{(9),\mathcal{Q}}(E_\pm) = {}& -\left(\frac{\pi}{3}\right)^{\frac{3}{2}} \frac{\Omega_{\mathrm{R}}^0}{\left|\Omega_{\mathrm{R}}^0\right|} E_\omega^2 E_{2\mathrm{q}+1} i^{-(L\pm1)} e^{i\left(\sigma_{L\pm}+\delta_{L\pm}+\phi_{2q+1}\right)} \langle Y_{L,M}|Y_{1,-1}\big|Y_{\lambda_2,\mu_2}\big\rangle\big\langle Y_{\lambda_2,\mu_2}\big|Y_{1,-1}\big|Y_{\lambda_1,\mu_1}\big\rangle\big\langle Y_{\lambda_1,\mu_1}\big|Y_{1,1}|Y_{1,1}\rangle \\ & \times \sum\!\!\!\!\!\!\!\int_{\nu_1,\nu_2} \frac{\langle R_{E_\pm,L}|r\big|R_{\nu_2,\lambda_2}\big\rangle\big\langle R_{\nu_2,\lambda_2}\big|r\big|R_{\nu_1,\lambda_1}\big\rangle\big\langle R_{\nu_1,\lambda_1}\big|r|R_{2,1}\rangle}{\left(\omega_{2p} \pm \frac{\left|\Omega_{\mathrm{R}}^0\right|}{2} + \Omega_{2q+1} - \omega - \omega_{\nu_2}\right)\left(\omega_{2p} \pm \frac{\left|\Omega_{\mathrm{R}}^0\right|}{2} + \Omega_{2q+1} - \omega_{\nu_1}\right)}, \end{aligned} \tag{25e}$$

where $\hat{O}_\Omega$ and $\hat{O}_\omega$ ($\hat{O}_\Omega^\dagger$ and $\hat{O}_\omega^\dagger$) are replaced by $-\sqrt{4\pi/3}rY_{1,1}(\hat{r})[\sqrt{4\pi/3}rY_{1,-1}(\hat{r})]$ for absorbing (emitting) each photon. Here the wave functions in Eqs. (21) are separated into their radial part and spherical harmonics in coordinate presentation: $\langle \vec{r}\,|\psi_{2s}\rangle = Y_{0,0}(\hat{r})R_{2,0}(r)$, $\langle \vec{r}\,|\psi_{2p}\rangle = Y_{1,1}(\hat{r})R_{2,1}(r)$, and $\langle \vec{r}\,|\psi_{\nu_i}\rangle = Y_{\lambda_i,\mu_i}(\hat{r})R_{\nu_i,\lambda_i}(r)$ with $\hat{r} = (\theta_r, \varphi_r)$.

In our calculation, for the two- and three-photon transition amplitudes in Eqs. (25), the infinite summation in the radial part is evaluated with the Dalgarno-Lewis method [68]. Then the radial part can be calculated using perturbed wave functions [69], which satisfy the inhomogeneous equation with its boundary conditions described in Ref. [70]. Particularly, the integration of two continuum wave functions appearing in Eqs. (25) is calculated by using the complex coordinate rotation method [71]. Additionally, verification of the matrix elements has been performed by the extrapolation method [72]. We select some numerical results of *dipole transition matrix elements* in Appendix D, where their radial and angular parts are separately shown.

IV. RESULTS

A. Case 1: Rabi-RABBITT using the left-hand circularly polarized XUV and IR fields

Figure 3(b) shows the populations of the $2s$ ($m = 0$), $2p$ ($m = 1$), and $3d$ ($m = 2$) states of the lithium atom as a function of the atom-field interaction time, which are approximately obtained by projecting the time-dependent TDSE solution to the eigenstates of the field-free Hamiltonian H_0 near the zero values of the vector potential of the external field. Within the dipole approximation, the time-dependent coefficients obtained by projecting the wave function onto the unperturbed eigenstates can be interpreted as probability amplitudes when using the full Hamiltonian written in the length gauge [73]. Moreover, when using the velocity gauge, the calculated projection coefficients coincide with those employing the length gauge *near the zeros of the vector potential* [74]. Here the intensities of the left-hand circularly polarized XUV and IR fields are 1×10^{13} and 1×10^{10} W/cm^2, respectively. As shown in Fig. 3(b), the populations of the $2s$ and $2p$ states oscillate out of phase with the interaction time, as a demonstration of Rabi oscillations [1]. As the IR intensity increases, the Rabi oscillations between the $2s$ and $2p$ states become faster, as shown in Figs. 3(c) and 3(d) for the IR intensities of 3×10^{10} and 1×10^{11} W/cm^2, respectively. As displayed in Fig. 3(a), the $3d$ ($m = 2$) state [the $3s$ state ($m = 0$)] is allowed (forbidden) to be populated through absorbing two IR photons from the $2s$ state ($m = 0$) according to the dipole selection rule $\Delta m = +1$ for the left-hand circular polarization. Due to the large detuning in the $2p - 3d$ transition, adopting the circular polarized IR field prevents the population leakage from the Rabi subspace $\mathcal{R}$, as shown in Figs. 3(b)–3(d).

During the entire interaction time, the Rabi oscillations shown in Figs. 3(b)–3(d) are smooth and uniform for the three IR intensities, respectively validating the rotating wave approximation in solving the Rabi amplitudes [Eq. (10)] and the monochromatic approximation for the IR field in Eqs. (21). Moreover, there is nearly no dampening in the Rabi oscillations for the three IR intensities due to the relatively negligible transition (including ionization) from $\mathcal{R}$ to $\mathcal{S}$, as indicated by the total population of the $2s$, $2p$, and $3d$ states after the laser pulses end in Figs. 3(b)–3(d). Therefore, it is a good approximation to treat the ionization *perturbatively* on the top of the Rabi wave function $\Psi_{\mathcal{R}}$ [Eq. (12)] which describes *perfectly* ongoing Rabi oscillations within $\mathcal{R}$ subspace. In addition, the incomplete Rabi oscillations are owing to the energy shifts

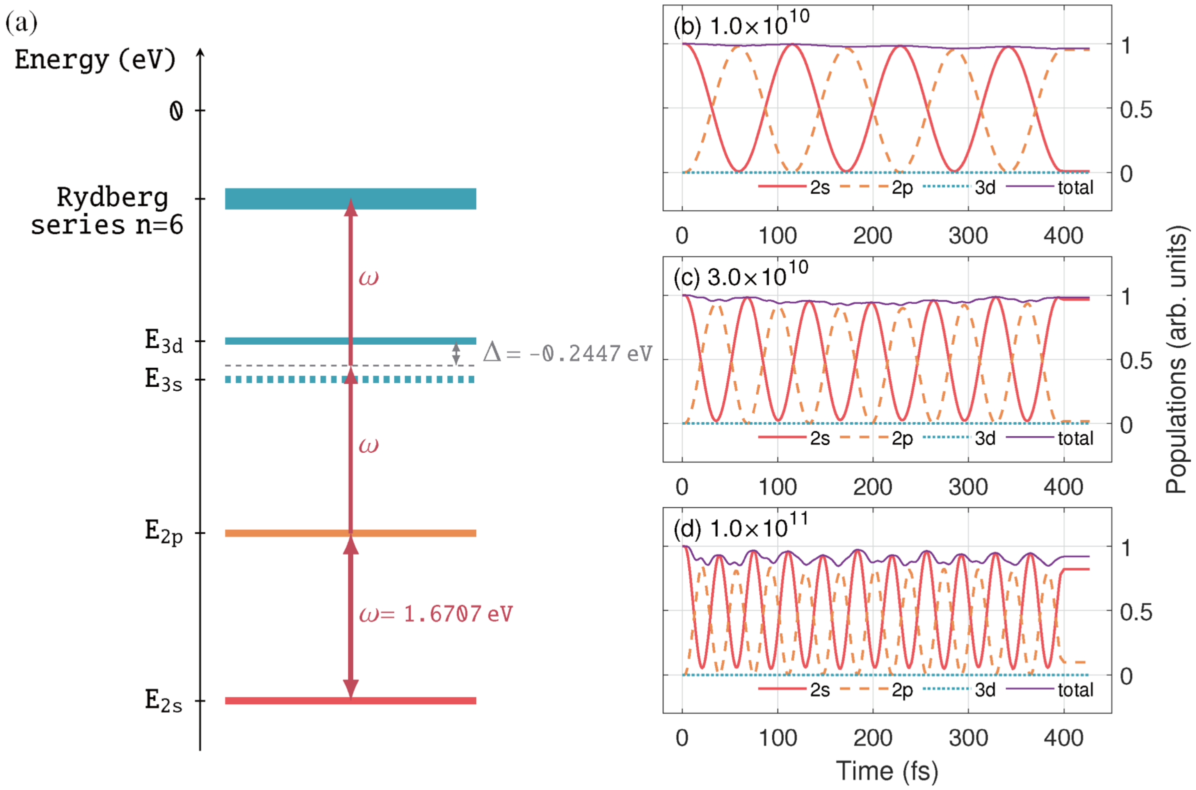

FIG. 3. (a) The schematic of the essential states of the lithium atom coupled to the IR field. The double-side (single-side) red arrows denote the strong (weak) coupling. The thick horizontal solid (dashed) lines indicate the states that are allowed (forbidden) to be populated according to the dipole selection rules. The detuning of the $2p-3d$ transition is $\Delta := \omega - E_{3d} + E_{2p}$, with E_{2p} and E_{3d} the energies of the $2p$ and $3d$ states of the lithium atom, respectively. (b)–(d) The populations of the $2s$ (red-solid lines), $2p$ (orange-dashed lines), $3d$ states of lithium (bluish-gray-dotted lines) and their summation (thin-purple-solid lines) as a function of the atom-field interaction time (the beginning time is set as zero). The intensities of the left-hand circularly polarized IR field are (b) 1×10^{10} (corresponding to the energy spacing of 0.0367 eV), (c) 3×10^{10} (corresponding to the energy spacing of 0.0642 eV), and (d) 1×10^{11} W/cm^2 (corresponding to the energy spacing of 0.1154 eV).

of the $2s$ and $2p$ states in the presence of the external fields, which are neglected in our analytical treatment owing to their small effects.

1. Comparison of TDSE and perturbation theory: RABBITT phases extracted from the photoelectron spectra within the polarization plane

Figure 4 shows the RABBITT phases as a function of photoelectron energy, which are extracted from the 2φ oscillation of SBs in the photoelectron spectra within the polarization plane of the XUV and IR fields. Note that the TDSE simulations and the perturbation theory (PT) calculations are performed in different coordinates without changing the physical observables. Here and hereafter the polarization plane refers to the xOy plane with $\theta = \pi/2$ as defined in the PT calculations. Figures 4(a1) and 4(a2) respectively show the RABBITT phases $\phi^{\mathrm{l}}(\pi/2)$ and $\phi^{\mathrm{h}}(\pi/2)$ of the peaks with the lower (P$^{\mathrm{l}}$) and higher (P$^{\mathrm{h}}$) energies in the AT doublet for the three IR intensities, which are calculated by solving the TDSE. Despite the tiny energy spacing between the AT doublet P$^{\mathrm{l}}$ and P$^{\mathrm{h}}$, $\phi^{\mathrm{l}}(\pi/2)$, and $\phi^{\mathrm{h}}(\pi/2)$ behave quite differently as a function of the photoelectron energy, which reveals the influence of the Rabi dynamics on the phase of the ionized electron wave packets. For both $\phi^{\mathrm{l}}(\pi/2)$ and $\phi^{\mathrm{h}}(\pi/2)$, their specific variations with the photoelectron energy rely on the IR intensity. In addition, $\phi^{\mathrm{l}}(\pi/2)$ and $\phi^{\mathrm{h}}(\pi/2)$ obviously show a change in its slope before and after SB 16. Figure 4(a3) shows the relative RABBITT phase $\Delta\phi(\pi/2) = \phi^{\mathrm{h}}(\pi/2) - \phi^{\mathrm{l}}(\pi/2)$ as a function of the photoelectron energy for the three IR intensities, which are obtained by solving the TDSE. For all the three IR intensities here, $\Delta\phi(\pi/2)$ varies in a similar way as the photoelectron energy and it is close to π. In addition, $\Delta\phi(\pi/2)$ deviates more from π for the higher IR intensity. Likewise, there is an obvious change in the slope of $\Delta\phi(\pi/2)$ around SB 16. Figures 4(b1), 4(b2), and 4(b3) respectively show the RABBITT phases $\phi^{\mathrm{l}}(\pi/2)$, $\phi^{\mathrm{h}}(\pi/2)$, and $\Delta\phi(\pi/2)$ calculated by PT including *all* pathways shown in Fig. 2 and using the same laser intensities and polarizations as the TDSE simulations. By comparing Figs. 4(b1), 4(b2), and 4(b3) separately with Figs. 4(a1), 4(a2), and 4(a3), their agreement validates the PT in Sec. III A on describing the physics process in the Rabi-RABBITT scheme for all the three IR intensities. In addition, the agreement between the PT and TDSE results are better at lower IR intensities when the Rabi oscillations within $\mathcal{R}$ are more accurately described by the zeroth-order wave function $\Psi_{\mathcal{R}}$ [Eq. (12)] due to smaller energy shifts of the $2s$ and $2p$ states, less population leakage to $\mathcal{S}$, and less dampening in the Rabi oscillations [Fig. 3].

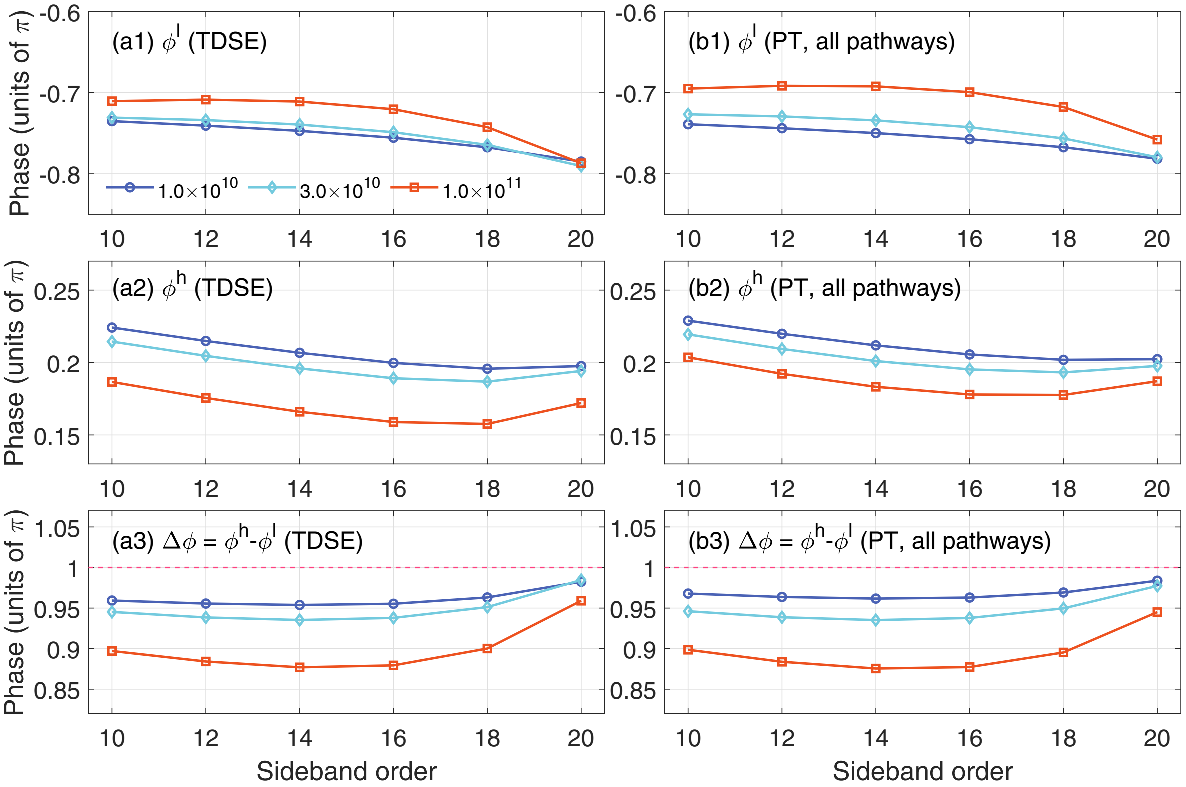

FIG. 4. From top to bottom: (a1), (b1) The RABBITT phases extracted from the photoelectron spectra within the polarization plane of the left-hand circularly polarized XUV and IR fields for P^l as a function of the photoelectron energy. (a2), (b2) The same as panels (a1), (b1), but for P^h. (a3), (b3) The relative RABBITT phases between P^h and P^l, as a function of the photoelectron energy. The different columns correspond to the results obtained (a1), (a2), (a3) by solving the TDSE and (b1), (b2), (b3) by perturbation theory including all pathways, respectively. The purple circles, blue rhombuses and orange squares correspond to the IR intensities of 1×10^{10}, 3×10^{10}, and 1×10^{11} W/cm^2, respectively.

To specifically reveal the underlying physics in the Rabi-RABBITT scheme, we analyze the PT results based on the two reduced subsets containing important ionization pathways in Fig. 2: *Subset five* consists of the *essential* pathways 1, 3, 5, 6, and 9; and *Subset three* is composed of pathways 1, 3, and 5. As a demonstration, Figs. 5(a) and 5(b) show the possible ionization channels of several essential pathways in *Case 1* and their relative strengths, which are determined by the dipole selection rules and the propensity rule in laser-assisted photoionization [75,76]. Pathway 1 has only one partial wave εd_2 (here and hereafter the continuum partial wave is denoted as εl_m with l the angular quantum number and m the magnetic quantum number) via one channel and pathway 3 has two partial waves εs_0 and εd_0 via two possible channels, as shown in Fig. 5(a). Pathway 5 (not shown) has the same partial wave as pathway 1. Pathway 6 has only one partial wave εg_4 via one channel and pathway 9 has three partial waves εs_0, εd_0, and εg_0 via four possible channels, as shown in Fig. 5(b).

The two rightmost columns in Fig. 5 show the RABBITT phases extracted from the 2φ oscillations of SBs in the photoelectron spectra within the polarization plane of the XUV and IR fields (xOy plane with $\theta = \pi/2$) as a function of the photoelectron energy, which are calculated by PT including part of pathways in Fig. 2 and using the same laser intensities and polarizations as the TDSE simulations. Figures 5(c1), 5(c2), and 5(c3) respectively show the RABBITT phases $\phi^l(\pi/2)$, $\phi^h(\pi/2)$, and $\Delta\phi(\pi/2)$ calculated only including pathways of *Subset five*, which exhibits an excellent agreement with the PT results including *all* pathways plotted in Figs. 4(b1), 4(b2), and 4(b3). Their further agreement with the TDSE results plotted in Figs. 4(a1), 4(a2), and 4(a3) indicates that the TDSE results can be accurately interpreted by only analyzing the interference among pathways of *Subset five*. Our calculations show that, in the formation of the 2φ-oscillation signal, the interference of pathways 3 and 5 has the most dominant contribution throughout all the photoelectron energy for the three IR intensities, followed by the interference of the usual RABBITT pathways 3 and 1 which has the second most important contribution. Furthermore, when comparing the phase of the 2φ-oscillation signal between the AT doublet P^l and P^h, the interference of pathways 3 and 5 (3 and 1) will give a π (zero) difference between the AT doublet P^l and P^h, recalling that there is a π difference between the initial phases of the electrons ionized from the dressed $2p$ states $|\phi^l_{2p}\rangle$ and $|\phi^h_{2p}\rangle$ due to the sine-like Rabi amplitude $\sin(\Omega^0_R t/2) \sim e^{i\Omega^0_R t/2} - e^{-i\Omega^0_R t/2}$ of the $2p$ state [Eq. (14)]. Therefore, the dominance of the interference of pathways 3 and 5 explains why $\Delta\phi(\pi/2)$ is very close to π throughout all photoelectron energies for all the three IR intensities as shown in Figs. 4(a3), 4(b3), and 5(c3), which is in qualitative accordance with the explanations only based on *Subset three* in Ref. [13]. In contrast with the Rabi-RABBITT scheme using the linearly polarized fields in Ref. [13], adopting the circularly polarized IR field prevents

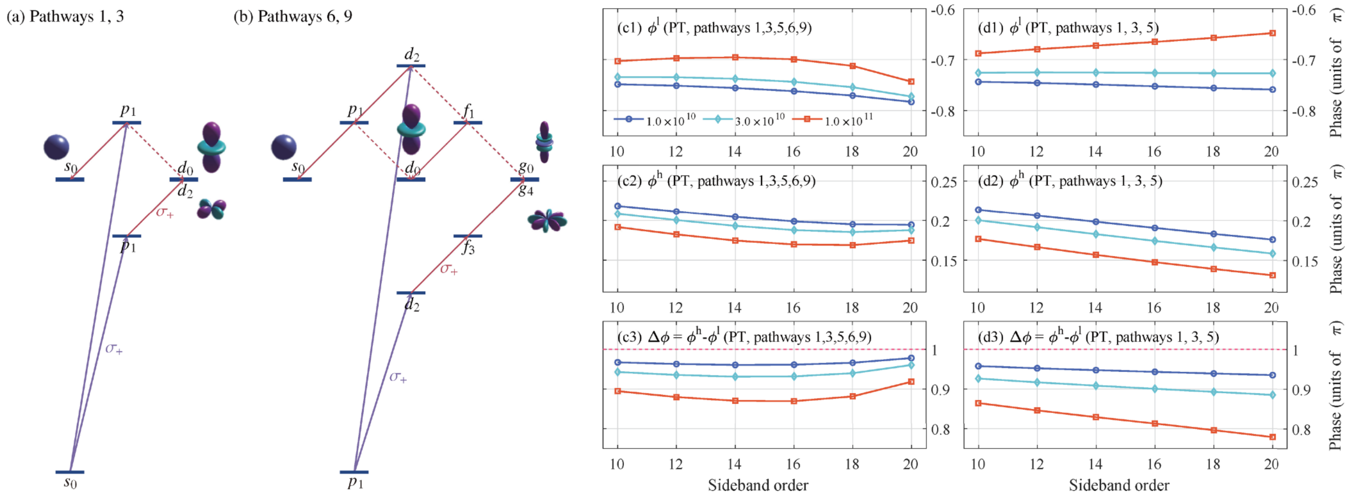

FIG. 5. (a) The schematic of the ionization channels for pathways 1 and 3 when using the left-hand circularly polarized (denoted σ_+) XUV and IR fields. (b) The same as panel (a), but for pathways 6 and 9. The purple and red arrows indicate the transition via exchanging the XUV and IR photons, respectively. The solid (dashed) arrows denote the relatively more (less) probable transition according to the propensity rule in laser-assisted photoionization when comparing each step of absorption and emission from the same state. The partial waves of each ionization channel are illustrated as the real spherical harmonics represented on polar plots. Pathway 5, having the same partial waves as pathway 1, is not shown. From top to bottom of the two rightmost columns: (c1), (d1) The RABBITT phases extracted from the photoelectron spectra within the polarization plane of the circularly polarized fields for P^{l} as a function of the photoelectron energy. (c2), (d2) The same as panels (c1), (d1), but for P^{h}. (c3), (d3) The relative RABBITT phases between P^{h} and P^{l}, as a function of the photoelectron energy. The different columns correspond to the results obtained by perturbation theory only including (c1), (c2), (c3) pathways 1, 3, 5, 6, 9 and (d1), (d2), (d3) pathways 1, 3, 5, respectively. The purple circles, blue rhombuses, and orange squares correspond to the IR intensities of 1×10^{10}, 3×10^{10}, and 1×10^{11} $\mathrm{W/cm^2}$, respectively.

the $3s$ ($m = 0$) from being populated and thus we have a more perfect two-level Rabi system within $\mathcal{R}$, as mentioned in the previous section. So here we aim to make a quantitative interpretation of the energy- and polar-angle-dependent RABBITT phases (time delays) including more processes.

For comparison, Figs. 5(d1), 5(d2), and 5(d3) respectively show the RABBITT phases $\phi^{\mathrm{l}}(\pi/2)$, $\phi^{\mathrm{h}}(\pi/2)$, and $\Delta\phi(\pi/2)$ calculated with only pathways of *Subset three* included. The RABBITT phases $\phi^{\mathrm{l}}(\pi/2)$, $\phi^{\mathrm{h}}(\pi/2)$, and $\Delta\phi(\pi/2)$ all change monotonically with the photoelectron energy for the three IR intensities. In particular, the relative phase $\Delta\phi(\pi/2)$ deviates more from π at higher photoelectron energies and for higher IR intensities because the relative contribution of the interference of pathways 3 and 1 with respect to that between pathways 3 and 5 increases with the photoelectron energy and with the IR intensity. This relatively increasing contribution of the interference between pathways 3 and 1 with *the photoelectron energy* results from a slower decline in the radial integral of the dipole moment matrix element associated with pathway 1 starting from the $2s$ state compared with that of pathway 5 initiated from the $2p$ state, as implied by the one-photon ionization cross sections from the $2s$ and $2p$ states for the photoelectron energies from 10 to 30 eV shown in Fig. 1. The relatively increasing contribution of the interference between pathways 3 and 1 with *the IR intensity* is attributed to a higher order of exchanging IR photons in the continuum for pathway 1 than pathway 5. Note that the photoelectrons with higher kinetic energies also interact more strongly with the laser field.

Compared with the monotonic tendencies of $\phi^{\mathrm{l}}(\pi/2)$, $\phi^{\mathrm{h}}(\pi/2)$, and $\Delta\phi(\pi/2)$ in the PT results for *Subset three*, the PT results for *Subset five* show some extra "bending" structures from SB 14 to SB 20 in the cases of $\phi^{\mathrm{l}}(\pi/2)$, $\phi^{\mathrm{h}}(\pi/2)$, and $\Delta\phi(\pi/2)$, which implies the non-negligible influence of the interference of pathways 5 with pathways 6 and 9. Indeed, our calculations indicate that these "bending" structures are attributed to the competition between the interference of pathways 5 and 6 versus the interference of pathways 1 and 3. Similar to the interference of pathways 1 and 3 both starting from the $2s$ state, the interference of pathways 5 and 6 both initiated from the $2p$ state also gives a zero difference in the phase of the 2φ oscillations between the AT doublet P^{l} and P^{h}. However, the interference between the zeroth-IR-order pathway 5 and the third-IR-order pathway 6 has an additional $\approx\pi$ phase compared with the interference between the two first-IR-order usual RABBITT pathways 1 and 3 due to the interaction phase shift accumulated during the absorption or emission of IR photons in multiphoton above-threshold ionization [77]. In this sense, the interference of pathways 5 and 6 will cancel in strength with the interference of pathways 1 and 3. As the photoelectron energy increases, the strength of the interference between pathways 5 and 6 becomes more comparable with (but still *weaker* than) the interference of pathways 1 and 3 from SB 16 to SB 20 for the three IR intensities, which is mainly determined by the relative amplitudes of the absorbed XUV harmonics in pathways 3 and 6 [e.g., E_{2q-3}, E_{2q-1}, and E_{2q+1} for $\mathrm{SB}_{2\mathrm{q}}$ in Eqs. (21)]. Hence, the summed strength of the interferences of pathways 1, 3 and of pathways 5, 6 increases from SB 10 to SB 14 and then decreases from SB 16 to SB 20. Recall that the most dominant interference of pathways 3 and 5 contributes a *Rabi π phase* in the formation of the 2φ oscillations between the AT doublet P^{l} and P^{h}. As a

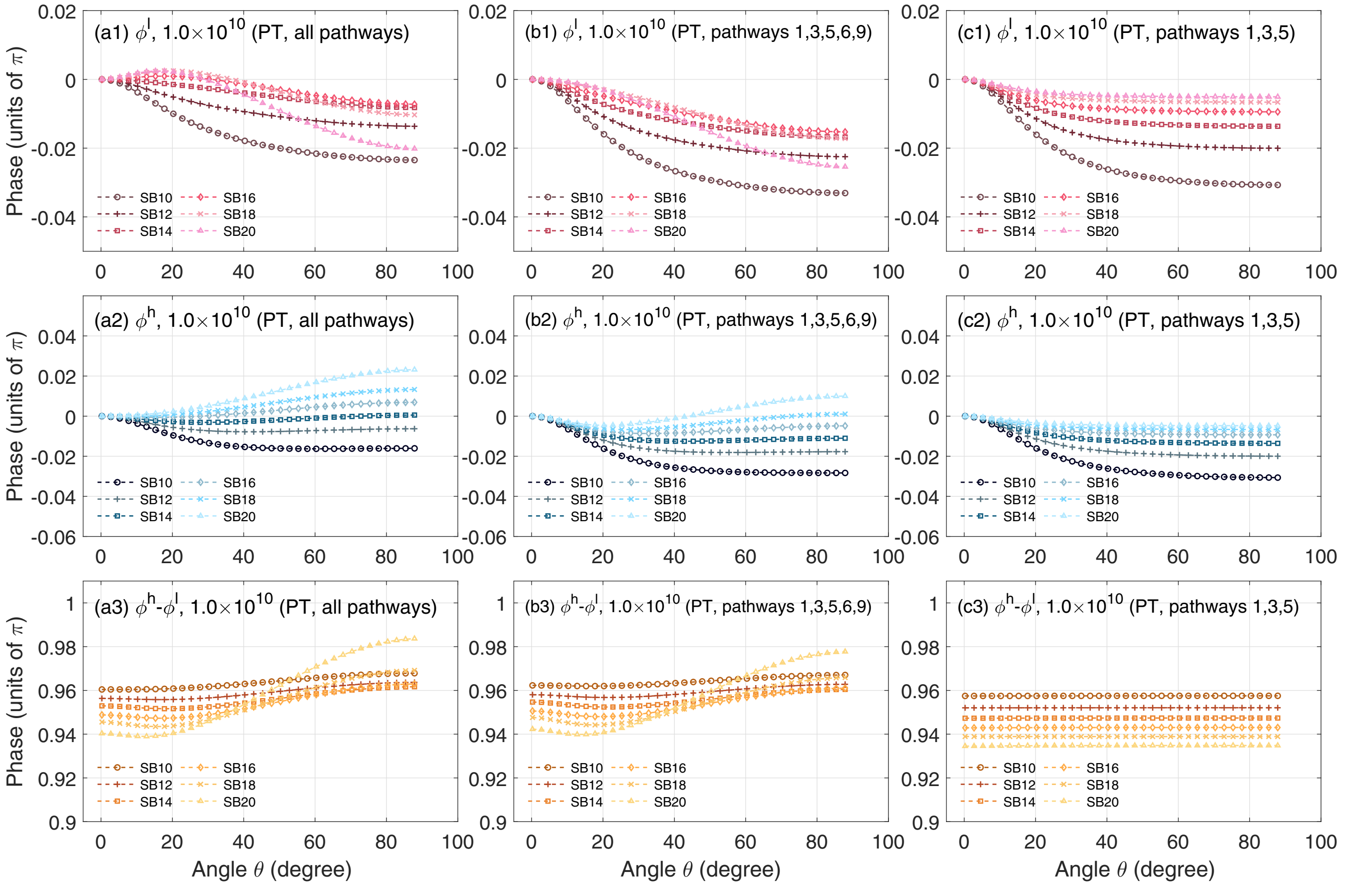

FIG. 6. From top to bottom: (a1), (b1), (c1) The relative polar-angle-resolved RABBITT phases for P^l as a function of polar emission angle of photoelectrons, with the intensities of the left-hand circularly polarized XUV and IR fields 1×10^{13} and 1×10^{10} W/cm^2, respectively. (a2), (b2), (c2) The same as (a1), (b1), (c1), but for P^h. (a3), (b3), (c3) The relative phases between P^h and P^l, as a function of the polar emission angle of photoelectrons. The different columns respectively correspond to the results obtained by perturbation theory including (a1), (a2), (a3) all pathways; (b1), (b2), (b3) only pathways 1, 3, 5, 6, and 9; and (c1), (c2), (c3) only pathways 1, 3, and 5. The circles, pluses, squares, rhombuses, crosses and triangles correspond to SBs 10, 12, 14, 16, 18 and 20, respectively.

superposition effect of the three pairs of interferences among pathways 1, 3, 5, and 6, $\Delta\phi(\pi/2)$ is near π while it is driven further from π from SB 10 to SB 14 and then becomes closer to π from SB 16 to SB 20, as shown in Figs. 4(a3), 4(b3), and 5(c3).

2. *Detailed analysis of perturbation theory results: polar-angle-resolved RABBITT phases*

As shown in Sec. IV A 1, our PT in Sec. III A is reliable to quantitatively reproduce the TDSE results, especially for low IR intensities in *Case 1*. Compared with the TDSE simulations, PT has the advantage of specifying the amplitude and the phase of each ionization channel so that the essential processes can be accurately identified in order to uncover the underlying mechanism. In the following, we apply PT for more detailed examinations on the polar-angle-integrated and polar-angle-resolved RABBITT phases in *Case 1* (Sec. IV A 2) and *Case 2* (Sec. IV B). Our PT calculations for *Case 1* show that, the phases extracted from the 2φ oscillations in SBs of the polar-angle-integrated photoelectron spectra (polar-angle-integrated RABBITT phases) have similar behaviors as the RABBITT phases $\phi^l(\pi/2)$, $\phi^h(\pi/2)$, and $\Delta\phi(\pi/2)$ due to the similar competition among the essential pathways of *Subset five*. In this sense, only the polar-angle-resolved RABBITT phases for the lowest IR intensity will be discussed in this section.

Figure 6 shows the RABBITT phases as a function of polar emission angle θ of photoelectrons, which are extracted from the 2φ oscillation of SBs in the three-dimensional photoelectron spectra. Here the intensities of the left-hand circularly polarized XUV and IR fields are 1×10^{13} and 1×10^{10} W/cm^2, respectively. Figure 6(a1) [Fig. 6(a2)] shows the polar-angle-resolved RABBITT phases $\phi^l(\theta)$ [$\phi^h(\theta)$] of the peak P^l (P^h) in the AT doublet for SBs 10 to 20, which are calculated with *all* pathways in Fig. 2 included. The phases $\phi^l(\theta)$ and $\phi^h(\theta)$ are given relative to a small polar angle $\theta_0 = 0.25^\circ$. Note that only the partial waves associated with the zero magnetic quantum number ($M = 0$) contribute to the signal along the propagation direction ($\theta = 0^\circ$) in the photoelectron spectra and thus there is no 2φ oscillation for $\theta = 0^\circ$. The RABBITT phases $\phi^l(\theta)$ and $\phi^h(\theta)$ both gently vary with polar angle θ for all SBs. For each SB, the obvious and counterintuitive discrepancy between the behaviors of $\phi^l(\theta)$ and $\phi^h(\theta)$ as a function of polar angle θ uncovers the influence of the Rabi dynamics on the phase of the ionized electron wave packets. Besides, the specific behaviors of both $\phi^{\mathrm{l}}(\theta)$ and $\phi^{\mathrm{h}}(\theta)$ depend on the photoelectron energy. For SBs 10 to 14, $\phi^{\mathrm{l}}(\theta)$ and $\phi^{\mathrm{h}}(\theta)$ both change smoothly and monotonically with polar angle θ. For SBs 16 to 20, however, $\phi^{\mathrm{l}}(\theta)$ and $\phi^{\mathrm{h}}(\theta)$ both exhibit some fluctuations and bendings in the vicinities of $\theta = 20^\circ$ and $\theta = 80^\circ$ as a function of polar angle θ. In addition, the curvatures of their bendings depend on the photoelectron energy. Figure 6(a3) shows the relative RABBITT phases $\Delta\phi(\theta) = \phi^{\mathrm{h}}(\theta) - \phi^{\mathrm{l}}(\theta)$ as a function of polar angle θ for SBs 10 to 20. The relative phase $\Delta\phi(\theta)$ is close to π at all polar emission angles θ for all SBs and it increases with polar angle θ for all SBs. Similarly, $\Delta\phi(\theta)$ varies smoothly with polar angle θ for SBs 10 to 14 while $\Delta\phi(\theta)$ shows a downward and an upward bendings separately near $\theta = 20^\circ$ and $\theta = 80^\circ$ for SBs 14 to 20. In addition, the slope of the increase of $\Delta\phi(\theta)$ becomes sharper and the curvatures of the twice bendings become bigger as the photoelectron energy increases. Figures 6(b1), 6(b2), and 6(b3) respectively show the RABBITT phases $\phi^{\mathrm{l}}(\theta)$, $\phi^{\mathrm{h}}(\theta)$, and $\Delta\phi(\theta)$ as a function of polar angle θ for SBs 10 to 20, which are calculated with only pathways of *Subset five* included. By comparing the first two columns in Fig. 6, it is seen that *Subset five* can already reproduce well the results in the first column (including *all* pathways in Fig. 2) for both the location of the "bending" structures and their dependence on the photoelectron energy.

For comparison, we calculate the RABBITT phases $\phi^{\mathrm{l}}(\theta)$, $\phi^{\mathrm{h}}(\theta)$, and $\Delta\phi(\theta)$ for SBs 10 to 20 by only including pathways in *Subset three*, which are respectively shown in Figs. 6(c1), 6(c2), and 6(c3). In Figs. 6(c1) and 6(c2), $\phi^{\mathrm{l}}(\theta)$ and $\phi^{\mathrm{h}}(\theta)$ both decrease monotonically with polar angle θ. In Fig. 6(c3), $\Delta\phi(\theta)$ is flat as a function of polar angle θ for all SBs. Our calculations show that the interference between pathways 3 and 5 (3 and 1) has the most (second most) important contribution in the formation of the 2φ-oscillation signal throughout all emission polar angles θ for all SBs. This dominance of the interference between pathways 3 and 5 explains why $\Delta\phi(\theta)$ is close to a *Rabi* π *phase* throughout all emission polar angles θ for all SBs in Figs. 6(a3), 6(b3), and 6(c3), rather than the usual near zero RABBITT phase at high photoelectron energies in consideration of the interaction phase shift [77]. Furthermore, the relative strength of the interference between pathways 3 and 1 compared with that between pathways 3 and 5 increases with the photoelectron energy and thus $\Delta\phi(\theta)$ deviates more from π at higher photoelectron energies in Fig. 6(c3) [and at higher IR intensities (not shown)]. For each SB, because pathways 1 and 5 have the same partial wave εd_2, the relative strength of the interference between pathways 3 and 1 with respect to that between pathways 3 and 5 keeps constant as a function of polar angle θ and thus $\Delta\phi(\theta)$ is flat with polar angle θ in Fig. 6(c3).

The discrepancy between the two rightmost columns suggests that the interferences between pathways 5, 6 and between pathways 5, 9 are responsible for the observed "bending" structures in Figs. 6(a3) and 6(b3). Similarly to the interference of pathways 5 and 6, the interference of pathways 5 and 9 also gives a zero difference in the phase of the 2φ oscillations between the AT doublet P^{l} and P^{h} and it also cancels in strength with the interference of pathways 1 and 3 due to the π interaction phase existing in the third-IR-order pathway 9. At small polar angles θ, the amplitude of the partial wave εg_4 of pathway 6 is nearly zero [Fig. 5(b)] and so as the strength of the interference of pathways 5 and 6. Therefore, the behavior of $\Delta\phi(\theta)$ near $\theta = 20^\circ$ in Figs. 6(a3) and 6(b3) is mainly determined by the cancellation on the interference of pathways 1 and 3 by the interference of pathways 5 and 9, which depends on the relative strength of these two pairs of interferences. For SBs 10 and 12, the relative strength of the interference between pathways 5 and 9 monotonically increases with polar angle θ and thus there is no bending for SBs 10 and 12. For SBs 14 to 20, their relative strength shows a dip in the vicinity of $\theta = 20^\circ$ and this dip becomes deeper with the increasing photoelectron energy. Correspondingly, the curvatures of the downward bending around $\theta = 20^\circ$ are bigger at higher energies for SBs 14 to 20. At big polar angles θ, the interference of pathways 5 and 6 dominates over that of pathways 5 and 9 for SBs 16 to 20 (which is mainly determined by the relative amplitudes of the absorbed XUV harmonics). Hence, the upward shape of the bending structure near $\theta = 80^\circ$ for SBs 16 to 20 in Figs. 6(a3) and 6(b3) is mainly attributed to the cancellation on the interference of pathways 1 and 3 by the interference of pathways 5 and 6. For SBs 16 to 20, the relative strength of the interference between pathways 5 and 6 monotonically increases with polar angle θ and its increase becomes more gentle as θ approaches 80°. Moreover, the slope of its increase in their relative strength is sharper for the SBs at higher energies and thus the curvature of the upward bending near $\theta = 80^\circ$ is bigger with increasing photoelectron energy, as shown in Figs. 6(a3) and 6(b3). Note that for the emission pathways 3 and 9, the partial wave εd_0 (εg_0) has a node at $\theta \approx 54.58^\circ$ (two nodes at $\theta \approx 34.54^\circ$ and $\theta \approx 69.85^\circ$). Nevertheless, no abrupt phase jumps occur in the interference of pathway 3 with pathway 1 nor 5 because the εs_0 wave dominates over the εd_0 wave in pathway 3 according to the propensity rule in laser-assisted photoionization [75]. Likewise, in pathway 9 where two IR photons are emitted in the continuum, each step of emission favors decreasing the electron angular momentum [76] and thus there is also no phase jump in the interference between pathways 5 and 9.

B. Case 2: Rabi-RABBITT using the left-hand circularly polarized XUV field and right-hand circularly polarized IR field

As shown in Table II, the RABBITT phases can be retrieved from the 2φ oscillations of SBs when the circularly polarized IR field is used. According to the dipole selection rules, the ionization channels differ when changing the polarizations of the laser fields in the Rabi-RABBITT scheme and so do the behaviors of the RABBITT phases. As demonstrated in Sec. IV A, when the circularly polarized XUV and IR fields are corotating, the behaviors of the RABBITT phases are mainly determined by the interferences among pathways of *Subset five*. As a comparison, in this section, we apply PT to examine the polar-angle-resolved (Sec. IV B 1) and polar-angle-integrated (Sec. IV B 2) RABBITT phases in *Case 2* of Table II where the XUV and IR fields have opposite circular polarizations (counter-rotating).

1. Polar-angle-resolved RABBITT phases

As a demonstration, Figs. 7(a) and 7(b) show the possible ionization channels of several pathways in *Case 2* and

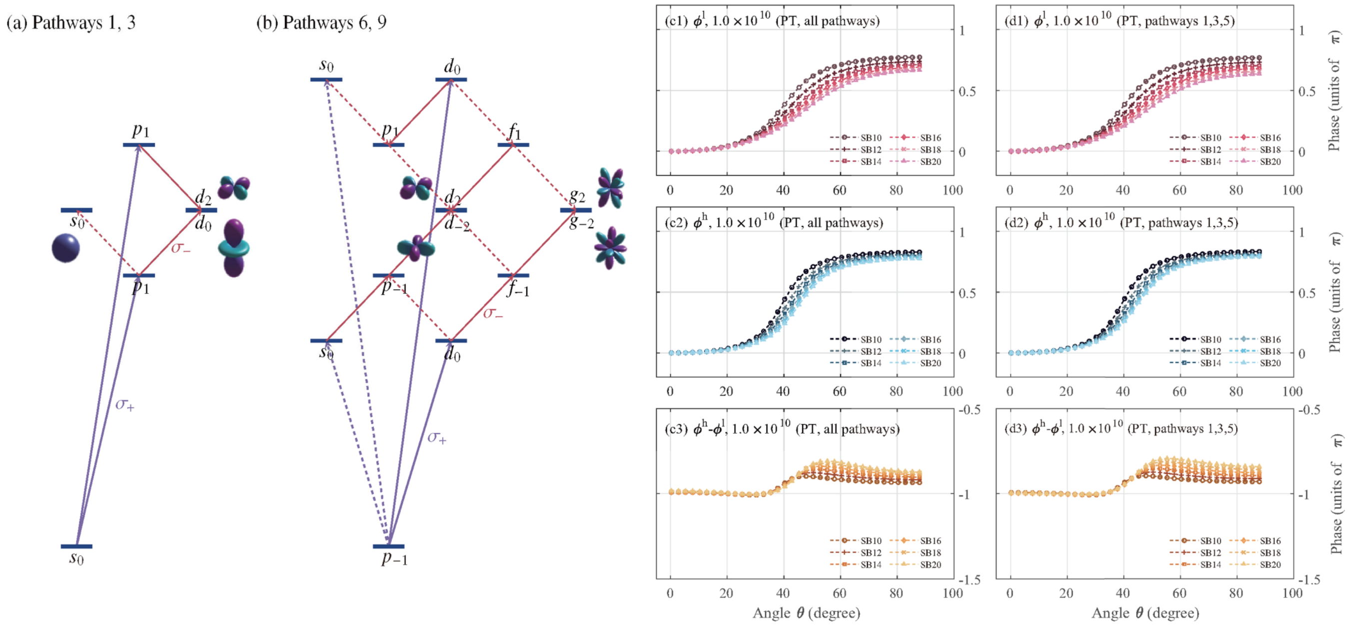

FIG. 7. (a) The schematic of the ionization channels for pathways 1 and 3 when using the left-hand circularly polarized (denoted σ_+) XUV field and the right-hand circularly polarized (denoted σ_-) IR field. (b) The same as panel (a), but for pathways 6 and 9. The purple and red arrows indicate the transition via exchanging the XUV and IR photons, respectively. The solid (dashed) arrows denote the relatively more (less) probable transition according to Fano's propensity rule and the propensity rule in laser-assisted photoionization when comparing each step of absorption and emission from the same state. The partial waves of each ionization channel are illustrated as the real spherical harmonics represented on polar plots. Pathway 5, having the same partial waves as pathway 1, is not shown. From top to bottom of the two rightmost columns: (c1), (d1) The polar-angle-resolved RABBITT phases for $\mathrm{P^l}$ as a function of polar emission angle of photoelectrons, with the intensities of the XUV and the IR fields 1×10^{13} and 1×10^{10} W/cm^2, respectively. (c2), (d2) The same as (c1), (d1), but for $\mathrm{P^h}$. (c3), (d3) The relative RABBITT phases between $\mathrm{P^h}$ and $\mathrm{P^l}$, as a function of the polar emission angle of photoelectrons. The different columns correspond to the results obtained by perturbation theory including (c1), (c2), (c3) all pathways and (d1), (d2), (d3) only pathways 1, 3, 5, respectively. The circles, pluses, squares, rhombuses, crosses and triangles correspond to SBs 10, 12, 14, 16, 18 and 20, respectively.

their relative strengths, which are determined by the dipole selection rules, Fano's propensity rule [78], and the propensity rule in laser-assisted photoionization [75,76]. Pathway 1 has two partial waves εs_0 and εd_0 via two possible channels and pathway 3 only has one partial wave εd_2 via one channel, as shown in Fig. 7(a). Pathway 5 (not shown) has the same two partial waves as pathway 1. Pathway 6 has two partial waves εd_{-2} and εg_{-2} via four possible channels and pathway 9 has two partial waves εd_2 and εg_2 via four possible channels, as shown in Fig. 7(b).

The two rightmost columns in Fig. 7 show the RABBITT phases as a function of polar emission angle θ of photoelectrons, which are extracted from the 2φ oscillations of SBs in the three-dimensional photoelectron spectra. Here the intensities of the left-hand circularly polarized XUV field and the right-hand circularly polarized IR field are 1×10^{13} and 1×10^{10} W/cm^2, respectively. Figure 7(c1) [Fig. 7(c2)] shows the polar-angle-resolved RABBITT phases $\phi^{\mathrm{l}}(\theta)$ [$\phi^{\mathrm{h}}(\theta)$] of the peak $\mathrm{P^l}$ ($\mathrm{P^h}$) in the AT doublet for SBs 10 to 20, which are calculated by including *all* pathways in Fig. 2. Here $\phi^{\mathrm{l}}(\theta)$ and $\phi^{\mathrm{h}}(\theta)$ are given relative to a small polar angle $\theta_0 = 0.25^\circ$. In contrast with corotating *Case 1*, when adopting the counterrotating XUV and IR fields in *Case 2*, $\phi^{\mathrm{l}}(\theta)$ and $\phi^{\mathrm{h}}(\theta)$ both exhibit an obvious phase jump around $\theta \approx 40^\circ$ for all SBs, as shown in Figs. 7(c1) and 7(c2). In addition, the steepness of the phase jump in $\phi^{\mathrm{h}}(\theta)$ is slightly sharper than that of $\phi^{\mathrm{l}}(\theta)$ for all SBs. For both $\phi^{\mathrm{l}}(\theta)$ and $\phi^{\mathrm{h}}(\theta)$, the steepness of the phase jump becomes more gentle and the amplitude of the phase jump becomes smaller with the increasing photoelectron energy. Figure 7(c3) shows the relative RABBITT phases $\Delta\phi(\theta) = \phi^{\mathrm{h}}(\theta) - \phi^{\mathrm{l}}(\theta)$ as a function of polar angle θ for SBs 10 to 20. For all SBs, the relative phase $\Delta\phi(\theta)$ is close to π and exhibits a phase jump of around 0.25π near $\theta \approx 40^\circ$. As the photoelectron energy increases, the amplitude of the phase jump in $\Delta\phi(\theta)$ becomes bigger.

Figures 7(d1), 7(d2), and 7(d3) respectively show the RABBITT phases $\phi^{\mathrm{l}}(\theta)$, $\phi^{\mathrm{h}}(\theta)$, and $\Delta\phi(\theta)$ calculated by only involving pathways in *Subset three*. The results agree excellently with the PT results including *all* pathways. This agreement implies that, in *Case 2*, only the interferences of pathway 3 with pathways 1 and 5 have the determinant influence on the behaviors of the RABBITT phases. Indeed, different from *Case 1* where pathways 5 and 6 only have a single partial wave (Fig. 5), pathways 5, 6, and 9 all have two partial waves in *Case 2*. More importantly, for each of pathways 5, 6, and 9 in *Case 2*, their two partial waves will interfere destructively due to the opposite signs of their dipole moment matrix elements originating from the angular integrals. Thus, the interferences of pathway 5 with pathways 6 and 9, as coherent summations of all the ionization channels, are negligible compared with that of the interferences of pathway 3 with pathways 1 and 5. Focusing on the interferences among pathways in *Subset three*, the interference of pathways 3 and 5 dominates over that of pathways 3 and 1 throughout

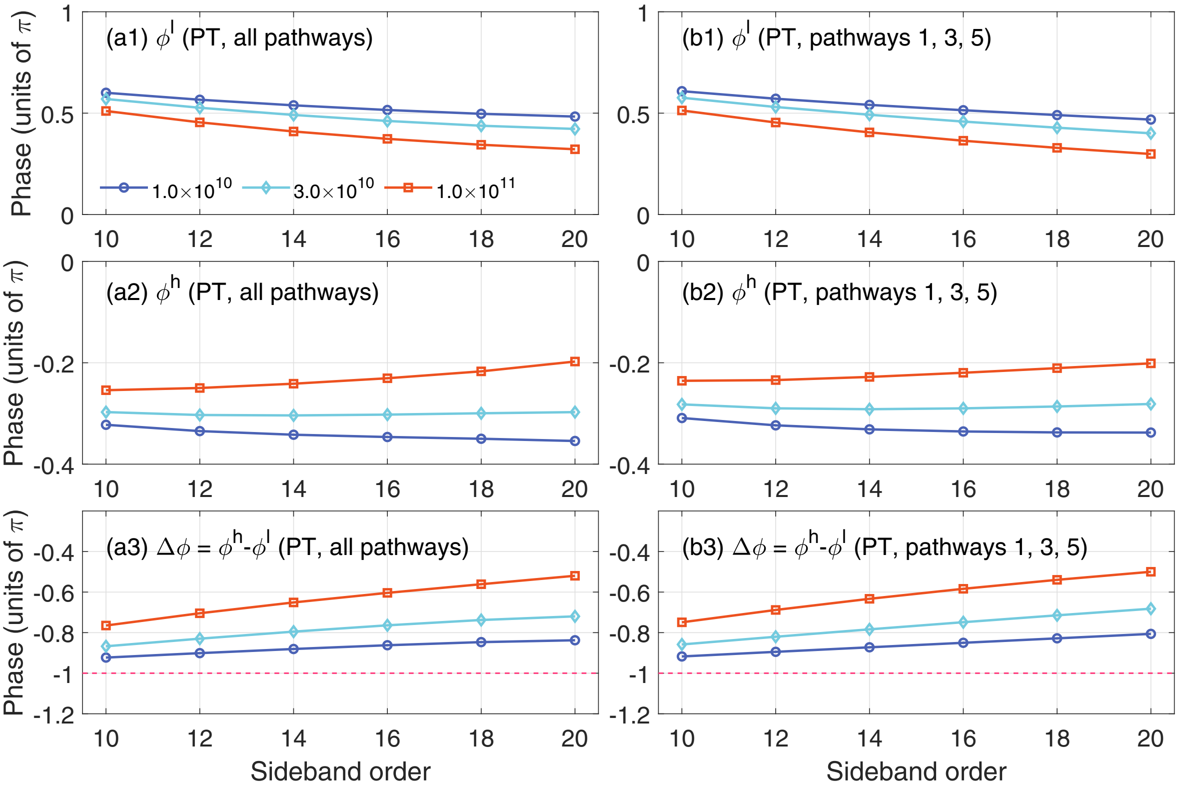

FIG. 8. From top to bottom: (a1), (b1) The polar-angle-integrated RABBITT phases for P^l as a function of the photoelectron energy. (a2), (b2) The same as panels (a1), (b1), but for P^h. (a3), (b3) The relative RABBITT phases between P^h and P^l, as a function of the photoelectron energy. The different columns correspond to the results obtained by perturbation theory including (a1), (a2), (a3) all pathways and (b1), (b2), (b3) only pathways 1, 3, and 5, respectively. The purple circles, blue rhombuses, and orange squares correspond to the IR intensities of 1×10^{10}, 3×10^{10}, and 1×10^{11} W/cm^2, respectively.

all polar angles θ for all SBs except in the vicinity of $\theta \approx 40^\circ$ where the interference of pathways 3 and 5 has a minimum in strength. Correspondingly, the relative phase $\Delta\phi(\theta)$ is close to a *Rabi* π *phase* in Figs. 7(c3) and 7(d3). In addition, the abrupt jumps of $\phi^l(\theta)$ and $\phi^h(\theta)$, respectively, in Figs. 7(d1) and 7(d2) for all SBs are attributed to the dominance of the εd_0 wave over the εs_0 wave in pathway 5 according to Fano's propensity rule favoring to increase angular quantum number in absorption of one photon from the dressed $2p$ states [78]. As the εd_0 wave changes its sign as a function of polar angle around its node $\theta \approx 54.5^\circ$, the εd_0 wave destructively (constructively) interferes with the nodeless εs_0 wave in pathway 5 at the angles smaller (bigger) than 54.5°, reminiscent of the *opposite* signs of the dipole moment matrix elements related to the εs_0 and εd_0 waves. Therefore, the phase jumps occur in the vicinity of $\theta = 40^\circ$ smaller than the εd_0 node at 54.5° where the interference between pathways 3 and 5 has a minimum in strength. Note that this differs from the case in Ref. [75] where the phase jumps locate around $\theta = 75^\circ$ larger than the εd_0 node at 54.5° because their εs_0 and εd_0 waves have the *same* signs when using the linearly polarized XUV and IR fields. In Figs. 7(d1) and 7(d2), no phase jump is observed for either $\phi^l(\theta)$ or $\phi^h(\theta)$ in the vicinity of $\theta = 15^\circ$ where the interference of pathways 3 and 1 has a minimum in strength due to its negligible contribution compared with the interference of pathways 3 and 5. Furthermore, the exact behaviors of the phase jumps are mainly determined by the relative strength and the phase of the interferences of pathway 3 with pathways 1 and 5. In particular, the slightly sharper steepness of the phase jump in $\phi^h(\theta)$ compared with that of $\phi^l(\theta)$ emphasizes the fact that there is a π difference between the initial phases of the electrons ionized from the dressed $2p$ states $|\phi^l_{2p}\rangle$ and $|\phi^h_{2p}\rangle$ [Eq. (14)].

2. *Polar-angle-integrated RABBITT phases*

Figure 8 shows the RABBITT phases as a function of the photoelectron energy, which are extracted from the 2φ oscillations in the photoelectron spectra integrated along polar emission angle θ of photoelectrons. Figures 8(a1) and 8(a2) respectively show the polar-angle-integrated RABBITT phases $\bar{\phi}^l$ and $\bar{\phi}^h$ of the peaks the AT doublet P^l and P^h in the AT doublet, which are calculated by including all pathways in Fig. 2. Here the intensity of the left-hand circularly polarized XUV field is 1×10^{13} W/cm^2. The intensities of the right-hand circularly polarized IR field are 1×10^{10}, 3×10^{10}, and 1×10^{11} W/cm^2, respectively. In Fig. 8(a1), $\bar{\phi}^l$ decreases with the photoelectron energy for the three IR intensities and it is less positive for the higher IR intensity. In Fig. 8(a2), $\bar{\phi}^h$ is less negative for the higher IR intensity and it shows a different dependence on the photoelectron energy for different IR intensities. At the highest (lowest) IR intensity, $\bar{\phi}^h$ increases (decreases) with the photoelectron energy. At the moderate IR intensity, $\bar{\phi}^h$ keeps nearly constant with the photoelectron energy. Figure 8(a3) shows the relative RABBITT phase $\Delta\bar{\phi} = \bar{\phi}^{\mathrm{h}} - \bar{\phi}^{\mathrm{l}}$ as a function of the photoelectron energy for the three IR intensities. For all the three IR intensities here, $\Delta\bar{\phi}$ is close to a *Rabi π phase* for all the photoelectron energies, which is explained by the dominance of the interference between pathways 3 and 5.

As a comparison, Figs. 8(b1), 8(b2), and 8(b3) respectively show the RABBITT phases $\bar{\phi}^{\mathrm{l}}$, $\bar{\phi}^{\mathrm{h}}$, and $\Delta\bar{\phi}$ calculated by only including pathways of *Subset three*, which shows an excellent agreement with the PT results including *all* pathways in Figs. 8(a1), 8(a2), and 8(a3). This agreement stresses the determinant roles of the interferences of pathway 3 with pathways 1 and 5 in *Case 2*. Furthermore, the relative contribution of the interference of pathways 1 and 3 with respect to that of pathways 3 and 5 increases with the photoelectron energy and with the IR intensity. Correspondingly, the relative phase $\Delta\bar{\phi}$ deviates more from a *Rabi π phase* at higher photoelectron energies and for higher IR intensities in Figs. 8(a3) and 8(b3). Moreover, the opposite dependence of the $\bar{\phi}^{\mathrm{l}}$ and $\bar{\phi}^{\mathrm{h}}$ on the photoelectron energy shown in Figs. 8(a2) and 8(b2) is attributed to the π difference between the initial phases of the electrons ionized from the dressed $2p$ states $|\phi_{2p}^{\mathrm{l}}\rangle$ and $|\phi_{2p}^{\mathrm{h}}\rangle$.

V. CONCLUSION

We have carefully examined the RABBITT technique applied to a Rabi-cycling atom by utilizing circularly polarized XUV and IR fields. In the RABBITT measurements, the circularly polarized IR field induced Rabi oscillations between the $2s$ and $2p$ states of lithium, which ensured *minimal* population leakage to the other bound states. Besides, the use of circularly polarized laser fields circumvented repetitive RABBITT measurements by scanning the time delay between the XUV and IR fields, which may make experimental verification more feasible for the proposed phase-matched *Cases 1 and 2*. In a single time-delay RABBITT measurement, the interference phase of the ionized electron wave packets was retrieved from the photoemission anisotropy along the azimuthal direction. As expected, both polar-angle-integrated and polar-angle-resolved photoelectron spectra exhibited a near π phase difference between each AT doublet, as a manifestation of the modulating populations of the two Rabi states [13]. In addition, adopting the circular polarizations exhibits a potential to steer the phase of the emitted electron wave packets by controlling the ionization channels. By using co- or counter-rotating XUV and IR fields, the polar-angle-integrated and polar-angle-resolved RABBITT phases exhibited different behaviors, which was traced back to different competition among partial waves determined by propensity rules [75,76,78]. In the corotating case, the polar-angle-integrated RABBITT phases showed a bending structure as a function of the photoelectron energy while the polar-angle-resolved RABBITT phases showed no phase jumps as a function of polar angle. These complex phenomena were captured by the competition among the essential ionization channels of *Subset five*. In the counter-rotating case, the polar-angle-integrated RABBITT phases varied monotonically with the photoelectron energy while the polar-angle-resolved RABBITT phases showed phase jumps near $\theta = 40^\circ$, which were explained by the competition among the essential ionization channels of *Subset three*.

We discussed how the interference pattern in photoelectron spectra encoded the information of the modulating populations of the two Rabi states. We believe the underlying physics can be generalized to the Rabi process studied by other similar interferometric schemes [79] and in more complicated molecular [80,81] and solid systems [82]. Besides, the pump-probe interferometry used here can also be adopted to investigate the modulating population in a multilevel system [83–85]. In addition, the analysis of the interference among multiple pathways is also applicable in other interferometric schemes [86–88].

Furthermore, the periodicity of the RABBITT process is determined by both the physical process of interest and the measurement process. In the RABBITT measurement on the autoionization process [89], the broken periodicity leads to a broadening [39] and a frequency modulation [90,91] of the spectral SB peaks. In the RABBITT measurement of Rabi oscillations, the periodic Rabi process manifests itself as a splitting of the observed SB peaks in the energy domain, and the periodicity of the RABBITT process is characterized commonly by the Rabi frequency and the laser probe frequency. When these two frequencies are incommensurable, there is no repetitive interference pattern as a function of the time delay between the two fields in the photoelectron spectra due to the nonperiodic RABBITT process. This breakdown of the periodicity becomes visible when the two SB peaks overlap in the AT doublet by using the laser fields with broader spectral widths (e.g., the Rainbow RABBITT method [39]). In this case, assuming the IR field is monochromatic, the modulations are like $|\Omega_{\mathrm{R}}^{0}|\tau$ within the overlap of the two SB peaks [11] while the modulations are like $2\omega\tau$ outside of their overlap according to Eqs. (21). Furthermore, the modulation frequency of SB peaks should include the finite-pulse effect [90,91] when both laser fields are spectrally broad.

ACKNOWLEDGMENTS

Y.L. acknowledges stimulating discussions with Z. Mašín, S. Patchkovskii, Z. Zhao, M. Bertolino, D. Busto, D. Hoff, and A. L'Huillier. This work was supported by National Key Research and Development Program of China (Grant No. 2019YFA0308300), National Natural Science Foundation of China (Grants No. 12374264, No. 12021004 and No. 92250303), and Shaanxi Science Foundation (Grant No. 2022JC-DW-05). J.M.D. acknowledges support from the Knut and Alice Wallenberg Foundation (Grant No. 2019.0154) and the Olle Engkvist's Foundation (Grant No. 194-0734). The computing work in this paper is supported by the Public Service Platform of High Performance Computing provided by Network and Computing Center of HUST.

APPENDIX A: SOLVING THE SCHRÖDINGER EQUATION WITHIN THE RABI SUBSPACE

In the two-level Rabi subspace $\mathcal{R}$, the Schrödinger equation is written as

$$i\frac{d}{dt}|\Psi_{\mathcal{R}}(t)\rangle = H_{\mathcal{R}}|\Psi_{\mathcal{R}}(t)\rangle, \tag{A1}$$

where the Hamiltonian $H_{\mathcal{R}}$ is defined in Eq. (9). The ansatz of this equation is a superposition of the $2s$ and $2p$ states,

$$|\Psi_{\mathcal{R}}(t)\rangle = C_{2s}(t;\tau)e^{-i\omega_{2s}t}|\psi_{2s}\rangle + C_{2p}(t;\tau)e^{-i\omega_{2p}t}|\psi_{2p}\rangle, \tag{A2}$$

which encodes the unitary transform $U_r = \exp(i\omega_{2s}t)|\psi_{2s}\rangle\langle\psi_{2s}| + \exp(i\omega_{2p}t)|\psi_{2p}\rangle\langle\psi_{2p}|$. In the condition at resonance $\omega = \omega_{2p} - \omega_{2s}$, the full transform can be decomposed into two successive unitary transforms as $U_r = S_0S_r$, where $S_0 = \exp[i(\omega_{2s} + \omega_{2p})t/2]\mathbb{I}$ subtracts the global energy offset $(\omega_{2s} + \omega_{2p})/2$ with $\mathbb{I} = |\psi_{2s}\rangle\langle\psi_{2s}| + |\psi_{2p}\rangle\langle\psi_{2p}|$ and where $S_r = \exp(i\omega\hat{\sigma}_z/2)$ encodes the change into a rotating frame [92,93] with $\hat{\sigma}_z = |\psi_{2s}\rangle\langle\psi_{2s}| - |\psi_{2p}\rangle\langle\psi_{2p}|$ the Pauli matrix for $\mathcal{R}$ subspace.

Inserting Eq. (A2) into Eq. (A1), the coefficient equations are obtained as

$$\frac{d}{dt}\bar{Y}(t) = \bar{A}(t)\bar{Y}(t), \tag{A3a}$$

where the coefficient matrix is

$$\bar{Y}(t) := \begin{pmatrix} C_{2s}(t;\tau) \\ C_{2p}(t;\tau) \end{pmatrix}, \tag{A3b}$$

and the interaction matrix is

$$\bar{A}(t) := -\frac{i}{2}\Omega_{\mathrm{R}}(t;\tau)\bar{M} \tag{A3c}$$

with the skew hermitian matrix

$$\bar{M} := \begin{pmatrix} 0 & e^{-i\omega\tau} \\ e^{i\omega\tau} & 0 \end{pmatrix}. \tag{A3d}$$

Note here that $\Omega_{\mathrm{R}}(t;\tau) = \Omega_{\mathrm{R}}^*(t;\tau)$ is used considering that $\Omega_{\mathrm{R}}(t;\tau)$ is real number. According to Magnus expansion [94], the solution of Eq. (A3a) is

$$\bar{Y}(t) = U'_{\mathcal{R}}(t,t_0)\bar{Y}(t_0), \tag{A4a}$$

with the propagator

$$\begin{aligned} &U'_{\mathcal{R}}(t,t_0) \\ &\quad = \exp\left(\int_{t_0}^{t}\bar{A}(t_1)dt_1 - \frac{1}{2}\int_{t_0}^{t}dt_1\int_{t_0}^{t_1}dt_2[\bar{A}(t_2),\bar{A}(t_1)] + \cdots\right). \end{aligned} \tag{A4b}$$

Here $U'_{\mathcal{R}}$ is the propagator corresponding to a unitary-transformed Hamiltonian $H'_{\mathcal{R}} = U_rH_{\mathcal{R}}U_r^\dagger - iU_r\partial_tU_r^\dagger$. Due to the commutation relation $[\bar{A}(t),\bar{A}(t')] = 0$, only the first-order term is kept in the exponential, i.e.,

$$\begin{aligned} U'_{\mathcal{R}}(t,t_0) &= \exp\left(\int_{t_0}^{t}\bar{A}(t')dt'\right) \\ &= \sum_{n=0}^{\infty}\frac{1}{n!}\left(\int_{t_0}^{t}\bar{A}(t')dt'\right)^n \\ &= \sum_{n=0}^{\infty}\frac{1}{n!}\left(-\frac{i}{2}\int_{t_0}^{t}\Omega_{\mathrm{R}}(t';\tau)dt'\right)^n\bar{M}^n. \end{aligned} \tag{A5}$$

Note that $\bar{M}$ satisfies

$$\bar{M}^n = \begin{cases} \bar{M}, & \text{for odd n} \\ \mathbb{I}, & \text{for even n,} \end{cases} \tag{A6}$$

and thus

$$\begin{aligned} U'_{\mathcal{R}}(t,t_0) = &\cos\left[\frac{1}{2}\int_{t_0}^{t}\Omega_{\mathrm{R}}(t';\tau)\,dt'\right]\mathbb{I} \\ &- i\sin\left[\frac{1}{2}\int_{t_0}^{t}\Omega_{\mathrm{R}}(t';\tau)\,dt'\right]\bar{M}. \end{aligned} \tag{A7}$$

Note that Eq. (A7) can also be derived from Eq. (A5) by directly using the relations

$$\bar{M} = \vec{\sigma}\cdot\hat{n}, \tag{A8a}$$

$$\begin{aligned} &\exp\left[-i\frac{1}{2}\int_{t_0}^{t}\Omega_{\mathrm{R}}(t';\tau)\,dt'\vec{\sigma}\cdot\hat{n}\right] \\ &\quad = \cos\left[\frac{1}{2}\int_{t_0}^{t}\Omega_{\mathrm{R}}(t';\tau)\,dt'\right]\mathbb{I} \\ &\qquad - i\sin\left[\frac{1}{2}\int_{t_0}^{t}\Omega_{\mathrm{R}}(t';\tau)\,dt'\right]\vec{\sigma}\cdot\hat{n}, \end{aligned} \tag{A8b}$$

where $\vec{\sigma} = [\hat{\sigma}_x,\hat{\sigma}_y,\hat{\sigma}_z]$ is related to Pauli matrices for $\mathcal{R}$ subspace and where $\hat{n} = [\cos(\omega\tau),\sin(\omega\tau),0]$ is the unity vector within the xOy plane in the representation of Bloch sphere [92,95,96].

Then the Rabi amplitudes in accordance with the area theorem [97] are given as

$$C_{2s}(t;\tau) = \cos\left[\frac{1}{2}\int_{t_0}^{t}\Omega_{\mathrm{R}}(t';\tau)dt'\right], \tag{A9a}$$

$$C_{2p}(t;\tau) = -ie^{i\omega\tau}\sin\left[\frac{1}{2}\int_{t_0}^{t}\Omega_{\mathrm{R}}(t';\tau)dt'\right], \tag{A9b}$$

which is obtained by using $\bar{Y}(t) = U'_{\mathcal{R}}(t,t_0)\bar{Y}(t_0)$ with $\bar{Y}(t_0)$ corresponding the boundary condition of $C_{2s}(t_0) = 1$ and $C_{2p}(t_0) = 0$. Here we take the initial time to infinity $t_0 \to -\infty$. Furthermore, the Fourier transform of the Rabi coefficients is defined as

$$\begin{aligned} \tilde{C}_{2s}(\omega_{\mathrm{R}};\tau) &:= \frac{1}{\sqrt{2\pi}}\int_{-\infty}^{\infty}C_{2s}(t;\tau)e^{-i\omega_{\mathrm{R}}t}d\omega_{\mathrm{R}} \\ &= \frac{1}{\sqrt{2\pi}}\int_{-\infty}^{\infty}\cos\left[\frac{1}{2}\int_{-\infty}^{t}\Omega_{\mathrm{R}}(t'-\tau)dt'\right] \\ &\quad\times e^{-i\omega_{\mathrm{R}}t}d\omega_{\mathrm{R}} \\ &= \frac{1}{\sqrt{2\pi}}\int_{-\infty}^{\infty}\cos\left[\frac{1}{2}\int_{-\infty}^{t-\tau}\Omega_{\mathrm{R}}(t')dt'\right] \\ &\quad\times e^{-i\omega_{\mathrm{R}}(t-\tau)}d\omega_{\mathrm{R}}e^{i\omega_{\mathrm{R}}\tau} \\ &= \tilde{C}_{2s}(\omega_{\mathrm{R}})e^{i\omega_{\mathrm{R}}\tau}, \end{aligned} \tag{A10a}$$

$$\begin{aligned} \tilde{C}_{2p}(\omega_{\mathrm{R}};\tau) &:= \frac{1}{\sqrt{2\pi}}\int_{-\infty}^{\infty}C_{2p}(t;\tau)e^{-i\omega_{\mathrm{R}}t}d\omega_{\mathrm{R}} \\ &= -\frac{ie^{i\omega\tau}}{\sqrt{2\pi}}\int_{-\infty}^{\infty}\sin\left[\frac{1}{2}\int_{-\infty}^{t}\Omega_{\mathrm{R}}(t'-\tau)dt'\right] \\ &\quad\times e^{-i\omega_{\mathrm{R}}t}d\omega_{\mathrm{R}} \\ &= \frac{-ie^{i(\omega+\omega_{\mathrm{R}})\tau}}{\sqrt{2\pi}}\int_{-\infty}^{\infty}\sin\left[\frac{1}{2}\int_{-\infty}^{t-\tau}\Omega_{\mathrm{R}}(t')dt'\right] \\ &\quad\times e^{-i\omega_{\mathrm{R}}(t-\tau)}d\omega_{\mathrm{R}} \\ &= \tilde{C}_{2p}(\omega_{\mathrm{R}})e^{i\omega_{\mathrm{R}}\tau}. \end{aligned} \tag{A10b}$$

APPENDIX B: DERIVATIONS OF THE DYSON SERIES IN THE RABI-RABBITT SCHEME

In verifying that the wave function $|\Psi(t)\rangle$ in Eq. (15) satisfies the Schrödinger equation

$$i\frac{d}{dt}|\Psi(t)\rangle = H(t)|\Psi(t)\rangle. \tag{B1}$$

We directly substitute into the Schrödinger equation by the ansatz [98,99]

$$|\Psi(t)\rangle = U(t,t_0)|\Psi(t_0)\rangle. \tag{B2a}$$

$$U(t,t_0) = U_{\mathcal{R}}(t,t_0) - i\int_{t_0}^{t} dt' U(t,t')H_{\text{int}}^{\perp\mathcal{R}}(t')U_{\mathcal{R}}(t',t_0). \tag{B2b}$$

Considering the initial condition $|\Psi_{\mathcal{R}}(t_0)\rangle = |\Psi(t_0)\rangle = e^{-i\omega_{2s}t_0}|\psi_{2s}\rangle$, we obtain

$$\begin{aligned}
i\frac{d}{dt}|\Psi(t)\rangle &= i\frac{d}{dt}U(t,t_0)|\Psi(t_0)\rangle \\
&= i\frac{d}{dt}U_{\mathcal{R}}(t,t_0)|\Psi_{\mathcal{R}}(t_0)\rangle + U(t,t)H_{\text{int}}^{\perp\mathcal{R}}(t)U_{\mathcal{R}}(t,t_0)|\Psi_{\mathcal{R}}(t_0)\rangle \\
&\quad - i\int_{t_0}^{t} dt' i\frac{d}{dt}U(t,t')H_{\text{int}}^{\perp\mathcal{R}}(t')U_{\mathcal{R}}(t',t_0)|\Psi_{\mathcal{R}}(t_0)\rangle - i\int_{t_0}^{t} dt' H(t)U(t,t')H_{\text{int}}^{\perp\mathcal{R}}(t')U_{\mathcal{R}}(t',t_0)|\Psi_{\mathcal{R}}(t_0)\rangle \\
&= \big[H_{\mathcal{R}}(t) + H_{\text{int}}^{\perp\mathcal{R}}(t)\big]U_{\mathcal{R}}(t,t_0)|\Psi_{\mathcal{R}}(t_0)\rangle - iH(t)\int_{t_0}^{t} dt' U(t,t')H_{\text{int}}^{\perp\mathcal{R}}(t')U_{\mathcal{R}}(t',t_0)|\Psi_{\mathcal{R}}(t_0)\rangle \\
&= H(t)\left[U_{\mathcal{R}}(t,t_0) - i\int_{t_0}^{t} dt' U(t,t')H_{\text{int}}^{\perp\mathcal{R}}(t')U_{\mathcal{R}}(t',t_0)\right]|\Psi_{\mathcal{R}}(t_0)\rangle \\
&= H(t)U(t,t_0)|\Psi(t_0)\rangle \\
&= H(t)|\Psi(t)\rangle.
\end{aligned} \tag{B3}$$

Note that in our derivation, we use

$$i\frac{d}{dt}|\Psi_{\mathcal{R}}(t)\rangle = H_{\mathcal{R}}(t)|\Psi_{\mathcal{R}}(t)\rangle, \tag{B4a}$$

$$|\Psi_{\mathcal{R}}(t)\rangle = U_{\mathcal{R}}(t,t_0)|\Psi_{\mathcal{R}}(t_0)\rangle, \tag{B4b}$$

$$i\frac{d}{dt}U_{\mathcal{R}}(t,t_0)|\Psi_{\mathcal{R}}(t_0)\rangle = H_{\mathcal{R}}(t)U_{\mathcal{R}}(t,t_0)|\Psi_{\mathcal{R}}(t_0)\rangle, \tag{B4c}$$

$$i\frac{d}{dt}U(t,t') = H(t)U(t,t'), \tag{B4d}$$

where the propagator of the full Hamiltonian is $U(t,t') := \hat{\mathcal{T}}\exp[-i\int_{t'}^{t} H(\tau)d\tau]$ with $\hat{\mathcal{T}}$ the time-ordering operator and $U(t,t) = 1$.

APPENDIX C: THE IONIZATION AMPLITUDES OF THE OTHER PATHWAYS

The ionization amplitudes $\mathcal{A}_{(i)}$ and their reduced amplitudes $\mathcal{M}_{(i),\mathcal{Q}}$ of pathways 2, 4, 7, 8, 10, and 11 in Fig. 2 are

$$\mathcal{A}_{(2)}(\vec{k}_\pm,\tau) = -\frac{i\pi}{4}e^{i[(\omega\pm\frac{|\Omega_{\text{R}}^0|}{2})\tau+\phi_{2q-1}]}E_{2\text{q}-1}E_\omega \mathop{\sum\!\!\!\!\!\!\!\int}_{\nu_1\neq 2p} \frac{\langle\psi_{f\pm}|\hat{O}_\Omega|\psi_{\nu_1}\rangle\langle\psi_{\nu_1}|\hat{O}_\omega|\psi_{2s}\rangle}{\omega_{2s}\pm\frac{|\Omega_{\text{R}}^0|}{2}+\omega-\omega_{\nu_1}}, \tag{C1a}$$

$$\mathcal{A}_{(4)}(\vec{k}_\pm,\tau) = -\frac{i\pi}{4}e^{-i[(\omega\mp\frac{|\Omega_{\text{R}}^0|}{2})\tau-\phi_{2q+1}]}E_{2\text{q}+1}E_\omega \mathop{\sum\!\!\!\!\!\!\!\int}_{\nu_1} \frac{\langle\psi_{f\pm}|\hat{O}_\Omega|\psi_{\nu_1}\rangle\langle\psi_{\nu_1}|\hat{O}_\omega^\dagger|\psi_{2s}\rangle}{\omega_{2s}\pm\frac{|\Omega_{\text{R}}^0|}{2}-\omega-\omega_{\nu_1}}, \tag{C1b}$$

$$\begin{aligned}
\mathcal{A}_{(7)}(\vec{k}_\pm,\tau) &= \mp\frac{i\pi}{8}\frac{\Omega_{\text{R}}^0}{|\Omega_{\text{R}}^0|}e^{i[(3\omega\pm\frac{|\Omega_{\text{R}}^0|}{2})\tau+\phi_{2q-3}]}E_\omega^2E_{2\text{q}-3} \\
&\quad\times\mathop{\sum\!\!\!\!\!\!\!\int}_{\nu_1,\nu_2} \frac{\langle\psi_{f\pm}|\hat{O}_\omega|\psi_{\nu_2}\rangle\langle\psi_{\nu_2}|\hat{O}_\Omega|\psi_{\nu_1}\rangle\langle\psi_{\nu_1}|\hat{O}_\omega|\psi_{2p}\rangle}{\big(\omega_{2p}\pm\frac{|\Omega_{\text{R}}^0|}{2}+\omega+\Omega_{2q-3}-\omega_{\nu_2}\big)\big(\omega_{2p}\pm\frac{|\Omega_{\text{R}}^0|}{2}+\omega-\omega_{\nu_1}\big)},
\end{aligned} \tag{C1c}$$

$$\begin{aligned}\mathcal{A}_{(8)}(\vec{k}_\pm,\tau)=&\mp\frac{i\pi}{8}\frac{\Omega_{\mathrm{R}}^0}{\left|\Omega_{\mathrm{R}}^0\right|}e^{i[(3\omega\pm\frac{|\Omega_{\mathrm{R}}^0|}{2})\tau+\phi_{2q-3}]}E_\omega^2E_{2\mathrm{q}-3}\\&\times\sum\!\!\!\!\!\!\int_{\nu_1,\nu_2}\frac{\langle\psi_{f\pm}|\hat{O}_\Omega|\psi_{\nu_2}\rangle\langle\psi_{\nu_2}|\hat{O}_\omega|\psi_{\nu_1}\rangle\langle\psi_{\nu_1}|\hat{O}_\omega|\psi_{2p}\rangle}{\left(\omega_{2p}\pm\frac{|\Omega_{\mathrm{R}}^0|}{2}+\omega+\omega-\omega_{\nu_2}\right)\left(\omega_{2p}\pm\frac{|\Omega_{\mathrm{R}}^0|}{2}+\omega-\omega_{\nu_1}\right)},\end{aligned}\tag{C1d}$$

$$\begin{aligned}\mathcal{A}_{(10)}(\vec{k}_\pm,\tau)=&\mp\frac{i\pi}{8}\frac{\Omega_{\mathrm{R}}^0}{\left|\Omega_{\mathrm{R}}^0\right|}e^{-i[(\omega\mp\frac{|\Omega_{\mathrm{R}}^0|}{2})\tau-\phi_{2q+1}]}E_\omega^2E_{2\mathrm{q}+1}\\&\times\sum\!\!\!\!\!\!\int_{\nu_1\neq2s,\nu_2}\frac{\langle\psi_{f\pm}|\hat{O}_\omega^\dagger|\psi_{\nu_2}\rangle\langle\psi_{\nu_2}|\hat{O}_\Omega|\psi_{\nu_1}\rangle\langle\psi_{\nu_1}|\hat{O}_\omega^\dagger|\psi_{2p}\rangle}{\left(\omega_{2p}\pm\frac{|\Omega_{\mathrm{R}}^0|}{2}-\omega+\Omega_{2q+1}-\omega_{\nu_2}\right)\left(\omega_{2p}\pm\frac{|\Omega_{\mathrm{R}}^0|}{2}-\omega-\omega_{\nu_1}\right)},\end{aligned}\tag{C1e}$$

$$\begin{aligned}\mathcal{A}_{(11)}(\vec{k}_\pm,\tau)=&\mp\frac{i\pi}{8}\frac{\Omega_{\mathrm{R}}^0}{\left|\Omega_{\mathrm{R}}^0\right|}e^{-i[(\omega\mp\frac{|\Omega_{\mathrm{R}}^0|}{2})\tau-\phi_{2q+1}]}E_\omega^2E_{2\mathrm{q}+1}\\&\times\sum\!\!\!\!\!\!\int_{\nu_1\neq2s,\nu_2}\frac{\langle\psi_{f\pm}|\hat{O}_\Omega|\psi_{\nu_2}\rangle\langle\psi_{\nu_2}|\hat{O}_\omega^\dagger|\psi_{\nu_1}\rangle\langle\psi_{\nu_1}|\hat{O}_\omega^\dagger|\psi_{2p}\rangle}{\left(\omega_{2p}\pm\frac{|\Omega_{\mathrm{R}}^0|}{2}-\omega-\omega-\omega_{\nu_2}\right)\left(\omega_{2p}\pm\frac{|\Omega_{\mathrm{R}}^0|}{2}-\omega-\omega_{\nu_1}\right)},\end{aligned}\tag{C1f}$$

$$\mathcal{M}_{(2),\mathcal{Q}}(E_\pm)=\frac{\pi}{3}E_{2\mathrm{q}-1}E_\omega i^{-(L+1)}e^{i\left(\sigma_{L\pm}+\delta_{L\pm}+\phi_{2q-1}\right)}\langle Y_{L,M}|Y_{1,1}|Y_{\lambda_1,\mu_1}\rangle\langle Y_{\lambda_1,\mu_1}|Y_{1,1}|Y_{0,0}\rangle\sum\!\!\!\!\!\!\int_{(\nu_1,\lambda_1)\neq2p}\frac{\langle R_{E_\pm,L}|r|R_{\nu_1,\lambda_1}\rangle\langle R_{\nu_1,\lambda_1}|r|R_{2,0}\rangle}{\omega_{2s}\pm\frac{|\Omega_{\mathrm{R}}^0|}{2}+\omega-\omega_{\nu_1}},\tag{C2a}$$

$$\begin{aligned}\mathcal{M}_{(4),\mathcal{Q}}(E_\pm)=&-\frac{\pi}{3}E_{2\mathrm{q}+1}E_\omega i^{-(L+1)}e^{i(\sigma_{L\pm}+\delta_{L\pm}+\phi_{2q+1})}\langle Y_{L,M}|Y_{1,1}|Y_{\lambda_1,\mu_1}\rangle\langle Y_{\lambda_1,\mu_1}|Y_{1,-1}|Y_{0,0}\rangle\\&\times\sum\!\!\!\!\!\!\int_{\nu_1}\frac{\langle R_{E_\pm,L}|r|R_{\nu_1,\lambda_1}\rangle\langle R_{\nu_1,\lambda_1}|r|R_{2,0}\rangle}{\omega_{2s}\pm\frac{|\Omega_{\mathrm{R}}^0|}{2}-\omega-\omega_{\nu_1}},\end{aligned}\tag{C2b}$$

$$\begin{aligned}\mathcal{M}_{(7),\mathcal{Q}}(E_\pm)=&-\left(\frac{\pi}{3}\right)^{\frac{3}{2}}\frac{\Omega_{\mathrm{R}}^0}{\left|\Omega_{\mathrm{R}}^0\right|}E_\omega^2E_{2\mathrm{q}-3}i^{-(L\pm1)}e^{i\left(\sigma_{L\pm}+\delta_{L\pm}+\phi_{2q-3}\right)}\langle Y_{L,M}|Y_{1,1}|Y_{\lambda_2,\mu_2}\rangle\langle Y_{\lambda_2,\mu_2}|Y_{1,1}|Y_{\lambda_1,\mu_1}\rangle\langle Y_{\lambda_1,\mu_1}|Y_{1,1}|Y_{1,1}\rangle\\&\times\sum\!\!\!\!\!\!\int_{\nu_1,\nu_2}\frac{\langle R_{E_\pm,L}|r|R_{\nu_2,\lambda_2}\rangle\langle R_{\nu_2,\lambda_2}|r|R_{\nu_1,\lambda_1}\rangle\langle R_{\nu_1,\lambda_1}|r|R_{2,1}\rangle}{\left(\omega_{2p}\pm\frac{|\Omega_{\mathrm{R}}^0|}{2}+\omega+\Omega_{2q-3}-\omega_{\nu_2}\right)\left(\omega_{2p}\pm\frac{|\Omega_{\mathrm{R}}^0|}{2}+\omega-\omega_{\nu_1}\right)},\end{aligned}\tag{C2c}$$

$$\begin{aligned}\mathcal{M}_{(8),\mathcal{Q}}(E_\pm)=&-\left(\frac{\pi}{3}\right)^{\frac{3}{2}}\frac{\Omega_{\mathrm{R}}^0}{\left|\Omega_{\mathrm{R}}^0\right|}E_\omega^2E_{2\mathrm{q}-3}i^{-(L\pm1)}e^{i\left(\sigma_{L\pm}+\delta_{L\pm}+\phi_{2q-3}\right)}\\&\times\langle Y_{L,M}|Y_{1,1}|Y_{\lambda_2,\mu_2}\rangle\langle Y_{\lambda_2,\mu_2}|Y_{1,1}|Y_{\lambda_1,\mu_1}\rangle\langle Y_{\lambda_1,\mu_1}|Y_{1,1}|Y_{1,1}\rangle\\&\times\sum\!\!\!\!\!\!\int_{\nu_1,\nu_2}\frac{\langle R_{E_\pm,L}|r|R_{\nu_2,\lambda_2}\rangle\langle R_{\nu_2,\lambda_2}|r|R_{\nu_1,\lambda_1}\rangle\langle R_{\nu_1,\lambda_1}|r|R_{2,1}\rangle}{\left(\omega_{2p}\pm\frac{|\Omega_{\mathrm{R}}^0|}{2}+\omega+\omega-\omega_{\nu_2}\right)\left(\omega_{2p}\pm\frac{|\Omega_{\mathrm{R}}^0|}{2}+\omega-\omega_{\nu_1}\right)},\end{aligned}\tag{C2d}$$

$$\begin{aligned}\mathcal{M}_{(10),\mathcal{Q}}(E_\pm)=&-\left(\frac{\pi}{3}\right)^{\frac{3}{2}}\frac{\Omega_{\mathrm{R}}^0}{\left|\Omega_{\mathrm{R}}^0\right|}E_\omega^2E_{2\mathrm{q}+1}i^{-(L\pm1)}e^{i\left(\sigma_{L\pm}+\delta_{L\pm}+\phi_{2q+1}\right)}\\&\times\langle Y_{L,M}|Y_{1,-1}|Y_{\lambda_2,\mu_2}\rangle\langle Y_{\lambda_2,\mu_2}|Y_{1,1}|Y_{\lambda_1,\mu_1}\rangle\langle Y_{\lambda_1,\mu_1}|Y_{1,-1}|Y_{1,1}\rangle\\&\times\sum\!\!\!\!\!\!\int_{(\nu_1,\lambda_1)\neq2s,\nu_2}\frac{\langle R_{E_\pm,L}|r|R_{\nu_2,\lambda_2}\rangle\langle R_{\nu_2,\lambda_2}|r|R_{\nu_1,\lambda_1}\rangle\langle R_{\nu_1,\lambda_1}|r|R_{2,1}\rangle}{\left(\omega_{2p}\pm\frac{|\Omega_{\mathrm{R}}^0|}{2}-\omega+\Omega_{2q+1}-\omega_{\nu_2}\right)\left(\omega_{2p}\pm\frac{|\Omega_{\mathrm{R}}^0|}{2}-\omega-\omega_{\nu_1}\right)},\end{aligned}\tag{C2e}$$

$$\begin{aligned}\mathcal{M}_{(11),\mathcal{Q}}(E_\pm)=&-\left(\frac{\pi}{3}\right)^{\frac{3}{2}}\frac{\Omega_{\mathrm{R}}^0}{\left|\Omega_{\mathrm{R}}^0\right|}E_\omega^2E_{2\mathrm{q}+1}i^{-(L\pm1)}e^{i\left(\sigma_{L\pm}+\delta_{L\pm}+\phi_{2q+1}\right)}\\&\times\langle Y_{L,M}|Y_{1,1}|Y_{\lambda_2,\mu_2}\rangle\langle Y_{\lambda_2,\mu_2}|Y_{1,-1}|Y_{\lambda_1,\mu_1}\rangle\langle Y_{\lambda_1,\mu_1}|Y_{1,-1}|Y_{1,1}\rangle\\&\times\sum\!\!\!\!\!\!\int_{(\nu_1,\lambda_1)\neq2s,\nu_2}\frac{\langle R_{E_\pm,L}|r|R_{\nu_2,\lambda_2}\rangle\langle R_{\nu_2,\lambda_2}|r|R_{\nu_1,\lambda_1}\rangle\langle R_{\nu_1,\lambda_1}|r|R_{2,1}\rangle}{\left(\omega_{2p}\pm\frac{|\Omega_{\mathrm{R}}^0|}{2}-\omega-\omega-\omega_{\nu_2}\right)\left(\omega_{2p}\pm\frac{|\Omega_{\mathrm{R}}^0|}{2}-\omega-\omega_{\nu_1}\right)}.\end{aligned}\tag{C2f}$$

TABLE III. The radial and angular integrals of the dipole transition matrix elements of pathways 1 to 11 for the higher-energy peak of SB 10 in *Case 1*.

Pathway	Ionization channel	Radial integral	Angular integral
1	$(l_i, \lambda_1, L) = (0, 1, 2)$	$41.031722524570355 + 53.198466268618446i$	0.365148371670111
2	$(l_i, \lambda_1, L) = (0, 1, 2)$	3.823833748129400	0.365148371670111
3	$(l_i, \lambda_1, L) = (0, 1, 0)$	$13.544666666666670 + 44.780000000000015i$	0.333333333333333
3	$(l_i, \lambda_1, L) = (0, 1, 2)$	$-12.984548602944278 - 11.427350863413425i$	−0.149071198499986
4	$(l_i, \lambda_1, L) = (0, 1, 0)$	−1.398733333333334	0.333333333333333
4	$(l_i, \lambda_1, L) = (0, 1, 2)$	0.852016435026670	−0.149071198499986
5	$(l_i, L) = (1, 2)$	0.213074268742145	0.632455532033676
6	$(l_i, \lambda_1, \lambda_2, L) = (1, 2, 3, 4)$	$4656.010341994734 + 3491.179677824839i$	0.276026223736942
7	$(l_i, \lambda_1, \lambda_2, L) = (1, 2, 3, 4)$	$4082.151822845632 + 1288.738836005407i$	0.276026223736942
8	$(l_i, \lambda_1, \lambda_2, L) = (1, 2, 3, 4)$	−839.4509516287872	0.276026223736942
9	$(l_i, \lambda_1, \lambda_2, L) = (1, 2, 1, 0)$	$-2362.517301523949 - 1025.027667919262i$	0.230940107675850
9	$(l_i, \lambda_1, \lambda_2, L) = (1, 2, 1, 2)$	$1004.238761782608 - 123.4397252103228i$	−0.103279555898864
9	$(l_i, \lambda_1, \lambda_2, L) = (1, 2, 3, 2)$	$277.7039715897753 - 23.54641086493669i$	−0.044262666813799
9	$(l_i, \lambda_1, \lambda_2, L) = (1, 2, 3, 4)$	$169.0151673747687 + 39.07506621875388i$	0.032991443953693
10	$(l_i, \lambda_1, \lambda_2, L) = (1, 0, 1, 0)$	$276.6854940046418 + 869.2200752739551i$	0.192450089729875
10	$(l_i, \lambda_1, \lambda_2, L) = (1, 0, 1, 2)$	$-256.6496964086782 - 221.8186661817862i$	−0.086066296582387
10	$(l_i, \lambda_1, \lambda_2, L) = (1, 2, 1, 0)$	$20.244209838865040 + 63.312230519334360i$	0.038490017945975
10	$(l_i, \lambda_1, \lambda_2, L) = (1, 2, 1, 2)$	$-17.338916109487684 - 16.156881592225183i$	−0.017213259316477
10	$(l_i, \lambda_1, \lambda_2, L) = (1, 2, 3, 2)$	$-219.8836499309096 + 75.62719251805706i$	−0.044262666813799
10	$(l_i, \lambda_1, \lambda_2, L) = (1, 2, 3, 4)$	$-98.482759346168690 - 11.215441372057903i$	0.032991443953693
11	$(l_i, \lambda_1, \lambda_2, L) = (1, 0, 1, 0)$	−21.007851794913194	0.192450089729875
11	$(l_i, \lambda_1, \lambda_2, L) = (1, 0, 1, 2)$	0.800098112918845	−0.086066296582387
11	$(l_i, \lambda_1, \lambda_2, L) = (1, 2, 1, 0)$	0.049998533311822	0.038490017945975
11	$(l_i, \lambda_1, \lambda_2, L) = (1, 2, 1, 2)$	−1.710240592647929	−0.017213259316477
11	$(l_i, \lambda_1, \lambda_2, L) = (1, 2, 3, 2)$	−4.063799702841705	−0.044262666813799
11	$(l_i, \lambda_1, \lambda_2, L) = (1, 2, 3, 4)$	−8.459336144166398	0.032991443953693

APPENDIX D: THE SELECTED NUMERICAL RESULTS OF THE DIPOLE TRANSITION MATRIX ELEMENTS

Table III gives the radial and angular integrals of the dipole transition matrix elements of pathways 1 to 11 in Fig. 2 for the photoelectron energy of $2q\omega - I_p^{2s} + \Omega_{\mathrm{R}}^0/2$ with $q = 5$ and $\Omega_{\mathrm{R}}^0 = 0.0367$ eV (the higher-energy peak of SB 10) in *Case 1*.

[1] I. I. Rabi, Phys. Rev. **51**, 652 (1937).

[2] G. Pileio, M. Carravetta, and M. H. Levitt, Phys. Rev. Lett. **103**, 083002 (2009).

[3] Y. O. Dudin, L. Li, F. Bariani, and A. Kuzmich, Nat. Phys. **8**, 790 (2012).

[4] S. Nandi, A. Stenquist, A. Papoulia, E. Olofsson, L. Badano, M. Bertolino, D. Busto, C. Callegari, S. Carlström, M. B. Danailov, arXiv:2312.04442.

[5] Y. Chen, Y. Zhou, Y. Li, M. Li, P. Lan, and P. Lu, Phys. Rev. A **97**, 013428 (2018).

[6] A. Batalov, C. Zierl, T. Gaebel, P. Neumann, I.-Y. Chan, G. Balasubramanian, P. R. Hemmer, F. Jelezko, and J. Wrachtrup, Phys. Rev. Lett. **100**, 077401 (2008).

[7] T. H. Stievater, X. Li, D. G. Steel, D. Gammon, D. S. Katzer, D. Park, C. Piermarocchi, and L. J. Sham, Phys. Rev. Lett. **87**, 133603 (2001).

[8] R. Merlin, Am. J. Phys. **89**, 26 (2021).

[9] P. Knight and P. Milonni, Phys. Rep. **66**, 21 (1980).

[10] S. H. Autler and C. H. Townes, Phys. Rev. **100**, 703 (1955).

[11] W.-C. Jiang, H. Liang, S. Wang, L.-Y. Peng, and J. Burgdörfer, Phys. Rev. Res. **3**, L032052 (2021).

[12] S. Nandi, E. Olofsson, M. Bertolino, S. Carlström, F. Zapata, D. Busto, C. Callegari, M. Di Fraia, P. Eng-Johnsson, R. Feifel, G. Gallician, M. Gisselbrecht, S. Maclot, L. Neoričić, J. Peschel, O. Plekan, K. C. Prince, R. J. Squibb, S. Zhong, P. V. Demekhin *et al.*, Nature (London) **608**, 488 (2022).

[13] Y. Liao, Y. Zhou, L.-W. Pi, J. Liang, Q. Ke, Y. Zhao, M. Li, and P. Lu, Phys. Rev. A **105**, 063110 (2022).

[14] X. Zhang, Y. Zhou, Y. Liao, Y. Chen, J. Liang, Q. Ke, M. Li, A. Csehi, and P. Lu, Phys. Rev. A **106**, 063114 (2022).

[15] E. Olofsson and J. M. Dahlström, Phys. Rev. Res. **5**, 043017 (2023).

[16] W.-C. Chu and C. D. Lin, Phys. Rev. A **87**, 013415 (2013).

[17] M. Wu, S. Chen, M. B. Gaarde, and K. J. Schafer, Phys. Rev. A **88**, 043416 (2013).

[18] C. Ott, A. Kaldun, L. Argenti, P. Raith, K. Meyer, M. Laux, Y. Zhang, A. Blättermann, S. Hagstotz, T. Ding, R. Heck, J. Madroñero, F. Martín, and T. Pfeifer, Nature (London) **516**, 374 (2014).

[19] N. Harkema, C. Cariker, E. Lindroth, L. Argenti, and A. Sandhu, Phys. Rev. Lett. **127**, 023202 (2021).

[20] N. F. Ramsey and R. W. Hellwarth, Phys. Today **p**(11), 37 (1956).

[21] G. Xu and D. J. Heinzen, Phys. Rev. A **59**, R922(R) (1999).

[22] G. Floquet, Ann. Sci. Ecole Norm. Sup. **12**, 47 (1883).

[23] S.-I. Chu and D. A. Telnov, Phys. Rep. **390**, 1 (2004).

[24] E. Jaynes and F. Cummings, Proc. IEEE **51**, 89 (1963).

[25] B. W. Shore and P. L. Knight, J. Mod. Opt. **40**, 1195 (1993).

[26] M. Hentschel, R. Kienberger, C. Spielmann, G. A. Reider, N. Milosevic, T. Brabec, P. Corkum, U. Heinzmann, M. Drescher, and F. Krausz, Nature (London) **414**, 509 (2001).

[27] P. M. Paul, E. S. Toma, P. Breger, G. Mullot, F. Augé, P. Balcou, H. G. Muller, and P. Agostini, Science **292**, 1689 (2001).

[28] R. Pazourek, S. Nagele, and J. Burgdörfer, Rev. Mod. Phys. **87**, 765 (2015).

[29] M. Isinger, R. J. Squibb, D. Busto, S. Zhong, A. Harth, D. Kroon, S. Nandi, C. L. Arnold, M. Miranda, J. M. Dahlström, E. Lindroth, R. Feifel, M. Gisselbrecht, and A. L'Huillier, Science **358**, 893 (2017).

[30] J. Liang, M. Han, Y. Liao, J.-b. Ji, C. S. Leung, W.-C. Jiang, K. Ueda, Y. Zhou, P. Lu, and H. J. Wörner, Nat. Photon. (2024), doi: 10.1038/s41566-023-01349-z.

[31] S. Beaulieu, A. Comby, A. Clergerie, J. Caillat, D. Descamps, N. Dudovich, B. Fabre, R. Géneaux, F. Légaré, S. Petit, B. Pons, G. Porat, T. Ruchon, R. Taïeb, V. Blanchet, and Y. Mairesse, Science **358**, 1288 (2017).

[32] M. Lucchini, L. Castiglioni, L. Kasmi, P. Kliuiev, A. Ludwig, M. Greif, J. Osterwalder, M. Hengsberger, L. Gallmann, and U. Keller, Phys. Rev. Lett. **115**, 137401 (2015).

[33] I. Jordan, M. Huppert, D. Rattenbacher, M. Peper, D. Jelovina, C. Perry, A. von Conta, A. Schild, and H. J. Wörner, Science **369**, 974 (2020).

[34] J. M. Dahlström, A. L'Huillier, and A. Maquet, J. Phys. B: At., Mol. Opt. Phys. **45**, 183001 (2012).

[35] J. M. Dahlström, D. Guénot, K. Klünder, M. Gisselbrecht, J. Mauritsson, A. L'Huillier, A. Maquet, and R. Taïeb, Chem. Phys. **414**, 53 (2013).

[36] E. S. Toma and H. G. Muller, J. Phys. B: At. Mol. Opt. Phys. **35**, 3435 (2002).

[37] V. Véniard, R. Taïeb, and A. Maquet, Phys. Rev. A **54**, 721 (1996).

[38] R. Géneaux, A. Camper, T. Auguste, O. Gobert, J. Caillat, R. Taïeb, and T. Ruchon, Nat. Commun. **7**, 12583 (2016).

[39] V. Gruson, L. Barreau, Á. Jiménez-Galan, F. Risoud, J. Caillat, A. Maquet, B. Carré, F. Lepetit, J.-F. Hergott, T. Ruchon, L. Argenti, R. Taïeb, F. Martín, and P. Salières, Science **354**, 734 (2016).

[40] S. Zhong, J. Vinbladh, D. Busto, R. J. Squibb, M. Isinger, L. Neoričić, H. Laurell, R. Weissenbilder, C. L. Arnold, R. Feifel, J. M. Dahlström, G. Wendin, M. Gisselbrecht, E. Lindroth, and A. L'Huillier, Nat. Commun. **11**, 5042 (2020).

[41] S. Biswas, B. Förg, L. Ortmann, J. Schötz, W. Schweinberger, T. Zimmermann, L. Pi, D. Baykusheva, H. A. Masood, I. Liontos, A. M. Kamal, N. G. Kling, A. F. Alharbi, M. Alharbi, A. M. Azzeer, G. Hartmann, H. J. Wörner, A. S. Landsman, and M. F. Kling, Nat. Phys. **16**, 778 (2020).

[42] X. Gong, W. Jiang, J. Tong, J. Qiang, P. Lu, H. Ni, R. Lucchese, K. Ueda, and J. Wu, Phys. Rev. X **12**, 011002 (2022).

[43] M. Swoboda, T. Fordell, K. Klünder, J. M. Dahlström, M. Miranda, C. Buth, K. J. Schafer, J. Mauritsson, A. L'Huillier, and M. Gisselbrecht, Phys. Rev. Lett. **104**, 103003 (2010).

[44] A. S. Kheifets, Phys. Rev. A **104**, L021103 (2021).

[45] A. Autuori, D. Platzer, M. Lejman, G. Gallician, L. Maëder, A. Covolo, L. Bosse, M. Dalui, D. Bresteau, J.-F. Hergott,, O. Tcherbakoff, H. J. B. Marroux, V. Loriot, F. Lépine, L. Poisson, R. Taïeb, J. Caillat, and P. Salières, Sci. Adv. **8**, eabl7594 (2022).

[46] S. Heuser, A. Jiménez Galán, C. Cirelli, C. Marante, M. Sabbar, R. Boge, M. Lucchini, L. Gallmann, I. Ivanov, A. S. Kheifets, J. M. Dahlström, E. Lindroth, L. Argenti, F. Martín, and U. Keller, Phys. Rev. A **94**, 063409 (2016).

[47] J. C. Baggesen and L. B. Madsen, Phys. Rev. Lett. **104**, 043602 (2010).

[48] R. Pazourek, J. Feist, S. Nagele, and J. Burgdörfer, Phys. Rev. Lett. **108**, 163001 (2012).

[49] M. Ossiander, F. Siegrist, V. Shirvanyan, R. Pazourek, A. Sommer, T. Latka, A. Guggenmos, S. Nagele, J. Feist, J. Burgdörfer, R. Kienberger, and M. Schultze, Nat. Phys. **13**, 280 (2017).

[50] S. Donsa, M. Ederer, R. Pazourek, J. Burgdörfer, and I. Březinová, Phys. Rev. A **102**, 033112 (2020).

[51] B. J. Sussman, Am. J. Phys. **79**, 477 (2011).

[52] O. Kfir, P. Grychtol, E. Turgut, R. Knut, D. Zusin, D. Popmintchev, T. Popmintchev, H. Nembach, J. M. Shaw, A. Fleischer, H. Kapteyn, M. Murnane, and O. Cohen, Nat. Photonics **9**, 99 (2015).

[53] S. Donsa, N. Douguet, J. Burgdörfer, I. Březinová, and L. Argenti, Phys. Rev. Lett. **123**, 133203 (2019).

[54] J. Sörngård, J. M. Dahlström, and E. Lindroth, J. Phys. B: At., Mol. Opt. Phys. **53**, 134003 (2020).

[55] M. Han, J.-B. Ji, T. Balčiūnas, K. Ueda, and H. J. Wörner, Nat. Phys. **19**, 230 (2023).

[56] A. Sarsa, F. Gálvez, and E. Buendía, At. Data Nucl. Data Tables **88**, 163 (2004).

[57] R. L. Kelly, J. Phys. Chem. Ref. Data **17** (1987), https://ui.adsabs.harvard.edu/abs/1987JPCRD..16S....K.

[58] T. N. Rescigno and C. W. McCurdy, Phys. Rev. A **62**, 032706 (2000).

[59] W.-C. Jiang and X.-Q. Tian, Opt. Express **25**, 26832 (2017).

[60] J. Liang, Y. Zhou, Y. Liao, W.-C. Jiang, M. Li, and P. Lu, Ultrafast Sci. **2022**, 9842716 (2022).

[61] D. G. Arbó, J. E. Miraglia, M. S. Gravielle, K. Schiessl, E. Persson, and J. Burgdörfer, Phys. Rev. A **77**, 013401 (2008).

[62] C. J. Joachain, N. J. Kylstra, and R. M. Potvliege, *Atoms in Intense Laser Fields* (Cambridge University Press, New York, 2011).

[63] K. Klünder, J. M. Dahlström, M. Gisselbrecht, T. Fordell, M. Swoboda, D. Guénot, P. Johnsson, J. Caillat, J. Mauritsson, A. Maquet, R. Taïeb, and A. L'Huillier, Phys. Rev. Lett. **106**, 143002 (2011).

[64] G. Breit and H. A. Bethe, Phys. Rev. **93**, 888 (1954).

[65] S. Altshuler, Nuovo Cimento **3**, 246 (1956).

[66] A. F. Starace, Handbuch der Physik **6**, 1 (1982).

[67] G. B. Arfken and H. J. Weber, *Mathematical Methods for Physicists* (Academic Press, Boston, 1999).

[68] A. Dalgarno, J. T. Lewis, and D. R. Bates, Proc. R. Soc. A **233**, 70 (1955).

[69] L.-W. Pi and A. F. Starace, Phys. Rev. A **90**, 023403 (2014).

[70] M. Aymar and M. Crance, J. Phys. B: At. Mol. Phys. **14**, 3585 (1981).

[71] B. Gao and A. F. Starace, Comput. Phys. **1**, 70 (1987).

[72] E. Cormier and P. Lambropoulos, J. Phys. B: At., Mol. Opt. Phys. **28**, 5043 (1995).
[73] D. H. Kobe and A. L. Smirl, Am. J. Phys. **46**, 624 (1978).
[74] J. Vábek, H. Bachau, and F. Catoire, Phys. Rev. A **106**, 053115 (2022).
[75] D. Busto, J. Vinbladh, S. Zhong, M. Isinger, S. Nandi, S. Maclot, P. Johnsson, M. Gisselbrecht, A. L'Huillier, E. Lindroth, and J. M. Dahlström, Phys. Rev. Lett. **123**, 133201 (2019).
[76] M. Bertolino, D. Busto, F. Zapata, and J. M. Dahlström, J. Phys. B: At., Mol. Opt. Phys. **53**, 144002 (2020).
[77] M. Bertolino and J. M. Dahlström, Phys. Rev. Res. **3**, 013270 (2021).
[78] U. Fano, Phys. Rev. A **32**, 617 (1985).
[79] Y.-J. Mao, H.-B. Yao, M. He, Z.-H. Zhang, Y. Li, and F. He, Phys. Rev. A **108**, 053117 (2023).
[80] S. Pan, C. Hu, W. Zhang, Z. Zhang, L. Zhou, C. Lu, P. Lu, H. Ni, J. Wu, and F. He, Light: Sci. Appl. **12**, 35 (2023).
[81] Z. Sun and N. Lou, Phys. Rev. Lett. **91**, 023002 (2003).
[82] R. E. F. Silva and A. Jiménez-Galán, Phys. Rev. A **106**, 053103 (2022).
[83] Y. Wu, Phys. Rev. A **54**, 1586 (1996).
[84] M. Sargent and P. Horwitz, Phys. Rev. A **13**, 1962 (1976).
[85] X.-K. Song, Q. Ai, J. Qiu, and F.-G. Deng, Phys. Rev. A **93**, 052324 (2016).
[86] G. Laurent, W. Cao, H. Li, Z. Wang, I. Ben-Itzhak, and C. L. Cocke, Phys. Rev. Lett. **109**, 083001 (2012).
[87] D. Bharti, D. Atri-Schuller, G. Menning, K. R. Hamilton, R. Moshammer, T. Pfeifer, N. Douguet, K. Bartschat, and A. Harth, Phys. Rev. A **103**, 022834 (2021).
[88] P. K. Maroju, M. Di Fraia, O. Plekan, M. Bonanomi, B. Merzuk, D. Busto, I. Makos, M. Schmoll, R. Shah, P. R. Ribič, L. Giannessi, G. De Ninno, C. Spezzani, G. Penco, A. Demidovich, M. Danailov, M. Coreno, M. Zangrando, A. Simoncig, M. Manfredda *et al.*, Nat. Photon. **17**, 200 (2023).
[89] Z. X. Zhao and C. D. Lin, Phys. Rev. A **71**, 060702(R) (2005).
[90] A. Jiménez-Galán, L. Argenti, and F. Martín, Phys. Rev. Lett. **113**, 263001 (2014).
[91] A. Jiménez-Galán, F. Martín, and L. Argenti, Phys. Rev. A **93**, 023429 (2016).
[92] I. I. Rabi, N. F. Ramsey, and J. Schwinger, Rev. Mod. Phys. **26**, 167 (1954).
[93] C. Cohen-Tannoudji, B. Diu, and F. Laloe, *Quantum Mechanics* (Wiley-VCH, 1986), Vol. 1.
[94] S. Blanes, F. Casas, J. Oteo, and J. Ros, Phys. Rep. **470**, 151 (2009).
[95] M. Harutyunyan, F. Holweck, D. Sugny, and S. Guérin, Phys. Rev. Lett. **131**, 200801 (2023).
[96] B. T. Torosov and N. V. Vitanov, Phys. Rev. A **99**, 013402 (2019).
[97] J. Eberly, Opt. Express **2**, 173 (1998).
[98] D. B. Milošević, J. Math. Phys. **54**, 042101 (2013).
[99] S. Patchkovskii, J. Benda, D. Ertel, and D. Busto, Phys. Rev. A **107**, 043105 (2023).